

IN-06
148137
P.33

Flight and Wind-Tunnel Calibrations of a Flush Airdata Sensor at High Angles of Attack and Sideslip and at Supersonic Mach Numbers

Timothy R. Moes, Stephen A. Whitmore, and Frank L. Jordan, Jr.

(NASA-TM-104265) FLIGHT AND
WIND-TUNNEL CALIBRATIONS OF A FLUSH
AIRDATA SENSOR AT HIGH ANGLES OF
ATTACK AND SIDESLIP AND AT
SUPERSONIC MACH NUMBERS (NASA)
33 p

N93-19110

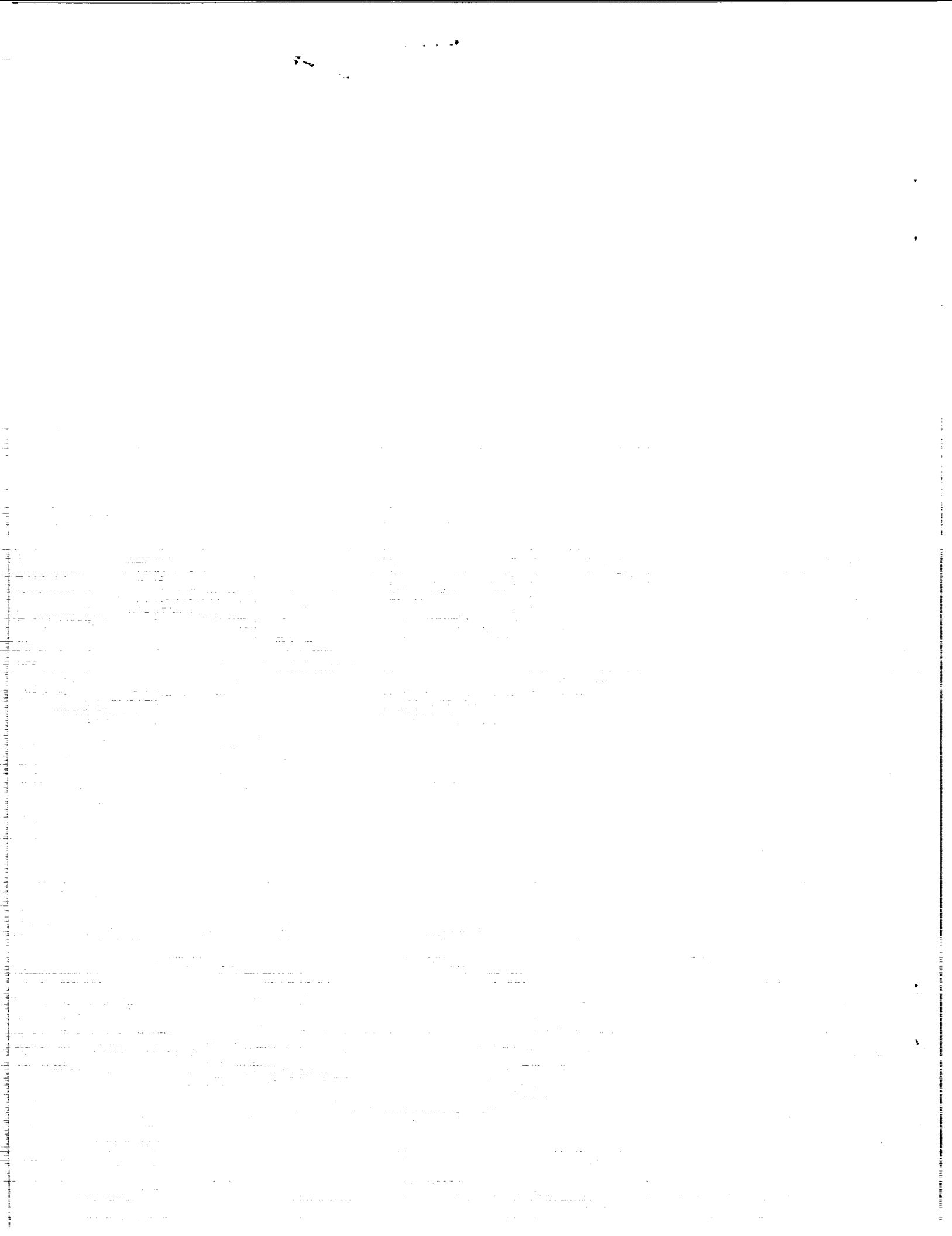
Unclass

G3/06 0148137

February 1993



National Aeronautics and
Space Administration



Flight and Wind-Tunnel Calibrations of a Flush Airdata Sensor at High Angles of Attack and Sideslip and at Supersonic Mach Numbers

Timothy R. Moes and Stephen A. Whitmore
Dryden Flight Research Facility,
Edwards, California

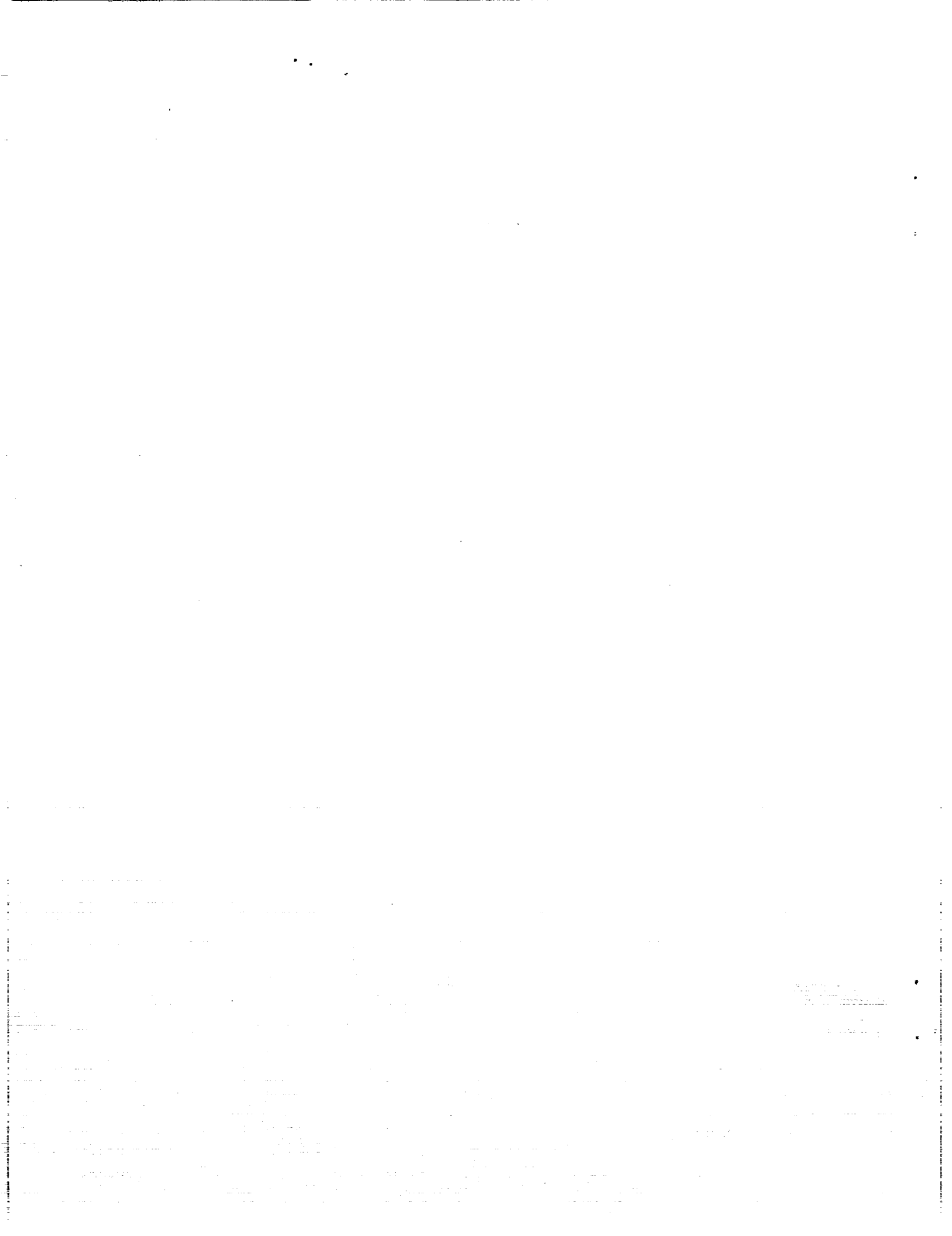
Frank L. Jordan, Jr.
Langley Research Center
Hampton, Virginia

1993



National Aeronautics and
Space Administration

Dryden Flight Research Facility
Edwards, California 93523-0273



FLIGHT AND WIND-TUNNEL CALIBRATIONS OF A FLUSH AIRDATA SENSOR AT HIGH ANGLES OF ATTACK AND SIDESLIP AND AT SUPERSONIC MACH NUMBERS

Timothy R. Moes* and Stephen A. Whitmore**
 NASA Dryden Flight Research Facility
 P.O. Box 273
 Edwards, California 93523-0273

Frank L. Jordan, Jr.†
 NASA Langley Research Center
 M/S 355
 Hampton, Virginia 23665-5225

Abstract

A nonintrusive airdata-sensing system has been calibrated in flight and wind-tunnel experiments to an angle of attack of 70° and to angles of sideslip of $\pm 15^\circ$. Flight-calibration data have also been obtained to Mach 1.2. The sensor, known as the flush airdata sensor, has been installed on the nose-cap of an F-18 aircraft for flight tests and on a full-scale F-18 forebody for wind-tunnel tests. Flight tests occurred at the NASA Dryden Flight Research Facility, Edwards, California, using the F-18 High Alpha Research Vehicle. Wind-tunnel tests were conducted in the 30-by 60-ft wind tunnel at the NASA Langley Research Center, Hampton, Virginia. The sensor consists of 23 flush-mounted pressure ports arranged in concentric circles and located within 1.75 in. of the tip of the nose-cap. An overdetermined mathematical model was used to relate the pressure measurements to the local airdata quantities. The mathematical model was based on potential flow over a sphere and was empirically adjusted based on flight and wind-tunnel data. For quasi-steady maneuvering, the mathematical model worked well throughout the subsonic, transonic, and low supersonic flight regimes. The model also worked well throughout the angles-of-attack and -sideslip regions studied.

Nomenclature

ESP electronically scanned pressure
 FADS flush airdata sensor

FS fuselage station, in.
 g acceleration of gravity ($1g = 32.2 \text{ ft/sec}^2$)
 HARV High Alpha Research Vehicle
 H_p pressure altitude, ft
 M free-stream Mach number
 p FADS surface pressure, psf
 p_∞ free-stream static pressure, psf
 q_c free-stream compressible dynamic pressure, psf
 \bar{q} free-stream incompressible dynamic pressure, psf
 \mathbf{R} pressure-port-position vector
 RMS root mean squared
 \mathbf{V} free-stream velocity vector
 α free-stream angle of attack, deg
 α_e effective angle of attack, deg
 α_F flank angle of attack, deg
 β free-stream angle of sideslip, deg
 β_e effective angle of sideslip, deg
 $\delta\alpha$ angle-of-attack calibration parameter, deg
 $\delta\alpha_{asy}$ asymmetric angle-of-attack calibration parameter, deg
 $\delta\alpha_{sym}$ symmetric angle-of-attack calibration parameter, deg
 $\delta\beta$ angle-of-sideslip calibration parameter, deg
 $\Delta\alpha$ angle-of-attack error, deg
 $\Delta\beta$ angle-of-sideslip error, deg
 ΔM Mach number error
 ΔH_p pressure-altitude error, ft

*Aerospace Engineer, Member AIAA.

**Senior Aerospace Engineer, Member AIAA.

†Aerospace Engineer, Member AIAA.

Copyright ©1993 by the American Institute of Aeronautics and Astronautics, Inc. No copyright is asserted in the United States under Title 17, U.S. Code. The U.S. Government has a royalty-free license to exercise all rights under the copyright claimed herein for Governmental purposes. All other rights are reserved by the copyright owner.

ϵ	calibration parameter
ϵ_M	component of ϵ as a function of Mach number
ϵ_α	component of ϵ as a function of angle of attack
ϵ_β	component of ϵ as a function of angle of sideslip
λ	FADS pressure port cone angle, deg
ϕ	FADS pressure port clock angle, deg
θ	flow-incidence angle, deg
F (...)	aerodynamic model functional

Subscripts

FADS	FADS airdata calculation
Flight	flight-derived calibrations
ref	reference airdata measurement
WT	wind-tunnel-derived calibrations

Introduction

Nonintrusive airdata-sensing systems are desirable for several aircraft design applications. The desire for low observability (stealth) has led to the incorporation of nonintrusive airdata systems on such aircraft as the B-2 bomber (Northrop Corporation, Newbury Park, California).¹ Nonintrusive airdata systems are required for hypersonic flight because of the high heat loads. In the 1960's, the X-15 aircraft (North American Aviation, Incorporated, Los Angeles, California) obtained airdata at speeds up to Mach 6.7 through the use of the nonintrusive ball-nose sensor. This innovative, yet complex, system consisted of five pressure ports and was hydraulically operated to align itself with the velocity vector at the nose of the aircraft.²

Today, the space shuttle does not typically measure airdata during the hypersonic portion of the descent. An intrusive sensor is extended for airdata measurements at speeds below Mach 3.5. However, because of a desire for airdata during the entire descent, the nonintrusive shuttle entry airdata system was flown and calibrated on five flights of Space Shuttle *Columbia*.³ This system avoided the complexity of the hydraulically operated ball-nose sensor by using a larger array of pressure measurements. The array consisted of 20 pressure measurements in a cruciform configuration on the nosecap and forward fuselage of the shuttle.

The National Aero-Space Plane program also funded research into nonintrusive hypersonic airdata systems. This research included pressure systems⁴ and optical airdata systems. Another area of interest for airdata system design is high-angle-of-attack flight which is increasingly used by fighter aircraft. Intrusive airdata

sensors alter the flow characteristics near the attachment point. For forebody installations, these changes in the airflow can strongly affect the stability and control of the vehicle at high angles of attack.⁵

This report describes the results of testing a nonintrusive pneumatic airdata sensor at high free-stream angles of attack, α , and sideslip, β , and at low supersonic Mach numbers. The sensor was designed for the nosecap of an F-18 aircraft (McDonnell Douglas Corporation, St. Louis, Missouri, and Northrop Corporation, Newbury Park, California). Flight and full-scale wind-tunnel data are presented for the flush airdata sensor (FADS). This sensor consists of 23 flush-mounted pressure ports arranged in concentric circles and located within 1.75 in. of the tip of the nosecap. An overdetermined mathematical model was used to relate the pressure measurements to the local airdata quantities.⁶ The mathematical model was based on potential flow over a sphere and included calibration parameters which could be empirically determined from flight and wind-tunnel data. Flight tests occurred at the NASA Dryden Flight Research Facility, Edwards, California, using the F-18 High Alpha Research Vehicle (HARV).⁷ Wind-tunnel tests were conducted in the 30- by 60-ft wind tunnel at NASA Langley Research Center, Hampton, Virginia.⁸

The research emphasis here is three-fold. A primary emphasis is to demonstrate the effectiveness of the wind tunnel for preliminary FADS system design and calibration. Flight development and calibration of airdata systems can be very elaborate and extensive. Wind tunnels potentially offer a simpler method for designing and calibrating FADS systems. A second emphasis is to demonstrate that the mathematical model developed from low-speed potential flow could also be directly used for obtaining airdata from the pressures at supersonic flight conditions. Flight results are given for speeds up to Mach 1.2. Lastly, this report will extend the FADS calibrations to angles of attack and sideslip beyond those shown in Ref. 6. Flight and wind-tunnel data are presented for angles of attack up to 70° and angles of sideslip to $\pm 15^\circ$.

Vehicle Description

Figure 1 shows the F-18 HARV, a modified F-18A single-place, twin-engine, fighter-attack aircraft. This aircraft features a variable-camber midwing with leading-edge extensions mounted on each side of the fuselage from the wing root to just forward of the cockpit. Control surfaces include ailerons, differential stabilators, twin rudders, and multiple flaps. The wingtip Sidewinder launch racks were removed and replaced with special camera pods that were also used to mount the wingtip research airdata booms.

Data presented here came from two phases of the HARV flight test program. In phase I, the left wingtip airdata boom consisted of a self-aligning pitot-static probe that aerodynamically aligned itself with the local velocity vector. Flow-direction vanes for angles of attack and sideslip were located aft of the pitot-static probe. The right wingtip airdata boom consisted of a stationary pitot-static probe and flow-direction vanes identical to those on the left wingtip.⁹ For phase II, self-aligning pitot-static probes were flown on both wingtips.

The major modification to the aircraft for phase II was the inclusion of a thrust-vectoring system.⁷ The system consisted of three paddles on each engine which were capable of redirecting the thrust vector. Use of these paddles was incorporated into the flight control system. The major benefit of the thrust vectoring was improved controllability of the aircraft at higher angles of attack. This improvement enabled steady-state flight at angles of attack up to 70° and allowed for the large sideslip angles necessary for this research. As a consequence of installing the thrust-vectoring system, the aircraft was limited to subsonic flight for phase II.

The basic FADS fixture is a small fiberglass-reinforced plastic cap that was blended into the metal flight test radome. The mold for the plastic cap was obtained from a production F-18 radome.

Wind-Tunnel Model Description

A full-scale F-18 forebody model was placed in the Langley 30- by 60-Foot Wind Tunnel (Fig. 2). The fiberglass model was constructed from splashes off of the HARV forward fuselage and from the same radome mold used to construct the flight FADS fixture. The forebody extends from the tip at fuselage station (FS) 59.82 to FS 190 and is capped with a faired afterbody. Fuselage station 190 is approximately where the canopy windscreen would begin on the F-18. Angle of attack was varied by actuating a hydraulic strut to pitch the model around a pivot point located slightly aft of FS 190. A floor-mounted turntable was rotated to obtain angle of sideslip. Note that the rotation angle of the turntable is not, by definition, the angle of sideslip, β , but is referred to as the flank angle of attack, α_F . The following equation was used to obtain true angle of sideslip:

$$\beta = \tan^{-1}[\cos(\alpha) \tan(\alpha_F)]$$

Sensor Description

The FADS pressure port configuration was identical on the flight vehicle and the wind-tunnel model. The FADS consisted of 23 flush-mounted pressure ports located between the forebody tip and FS 61.57 (Fig. 3). These ports were arranged in annular rings and had a 0.046 in. inside diameter. Each pressure port is located

using a cone angle, λ , and a clock angle, ϕ . Pressures at the nosecap were sensed using a 32-port electronically scanned pressure (ESP) module. Individually calibrated transducers in the ESP module measured differential pressure between the surface pressures and the pressure in a reference tank which was vented to the radome interior. Reference tank pressure was measured with a highly accurate absolute pressure transducer. Pneumatic tubing transported pressures at the surface to the ESP module. No appreciable time lags existed in the measured pressures caused by the pneumatic tubing geometry.⁶

Flow Analysis and Pressure Modeling

This section describes the aerodynamic model used to relate the FADS pressure measurements to the desired airdata quantities of α and β as well as free-stream static pressure and compressible dynamic pressure, p_∞ and q_c . With this model, all available FADS pressure measurements can be used simultaneously to estimate the airdata by means of an overdetermined nonlinear regression. Reference 6 describes the FADS aerodynamic model in detail. The model is based on potential flow for a three-dimensional doublet in uniform flow and expresses the surface pressure in terms of flow incidence angle, θ , and calibration parameter, ϵ , as

$$p(\theta) = q_c[\cos^2(\theta) + \epsilon \sin^2(\theta)] + p_\infty$$

To account for nonideal nose shape, compressibility, and afterbody effects, the calibration parameter ϵ is allowed to vary smoothly as a function of flight conditions.

The flow incidence angle, θ , may be written in terms of angle of attack and angle of sideslip by taking the inner product of the position vector (normal to the surface tangent) with the velocity vector

$$\begin{aligned} \cos(\theta) &= \mathbf{V} \cdot \mathbf{R} / \|\mathbf{V}\| \|\mathbf{R}\| \\ &= \cos(\alpha) \cos(\beta) \cos(\lambda) + \sin(\beta) \sin(\phi) \sin(\lambda) \\ &\quad + \sin(\alpha) \cos(\beta) \cos(\phi) \sin(\lambda) \end{aligned}$$

Therefore, for a given location on the surface

$$p(\phi, \lambda) = F(\alpha, \beta, q_c, p_\infty, \phi, \lambda, \epsilon)$$

where α , β , q_c , and p_∞ are the airdata parameters; ϕ and λ are the orifice coordinate angles; and ϵ is the calibration parameter yet to be empirically determined.

The potential flow model assumed a nonlifting sphere with no trailing afterbody. Clearly, this is not the case for the nose of an aircraft where vehicle-induced upwash and sidewash alter the local flow angles.¹⁰ Thus, the FADS system measured local or effective angles of attack and sideslip, α_e and β_e , and

not free-stream angles-of-attack and -sideslip (α and β). Effective and free-stream angles are related by

$$\alpha_e = \alpha + \delta\alpha$$

$$\beta_e = \beta + \delta\beta$$

where angles-of-attack and -sideslip calibrated parameters, $\delta\alpha$ and $\delta\beta$, are factors that must also be empirically identified.

Calibration Techniques

A true airdata reference set is required for the calibration of the aerodynamic model. For the wind-tunnel data, airdata reference conditions can be determined from tunnel calibrations. Corrections were applied to the tunnel data to account for the influence of the support apparatus. Reference airdata for the flight test maneuvers were obtained from the calibrated wingtip airdata probes.

The wind-tunnel calibration of the FADS system consisted of angle-of-attack sweeps at 0° sideslip and angle-of-sideslip sweeps at set angles of attack. The following table shows the run schedule for the wind-tunnel tests:

Run	α , deg	β , deg	\bar{q} , psf
365	Basic α sweep ^a	0	4
366	Basic α sweep ^a	0	8
409	Extended α sweep ^b	0	12
428	30	β sweep ^c	12
430	32	β sweep ^c	12
432	36	β sweep ^c	12

^aBasic α sweep, deg: -8, -4, 0, 4, 8, 12, 16, 20, 24, 28, 32, 36, 40, 44, 48, 52, 56, 60, 64, 68, 72, 76, 80

^bExtended α sweep, deg: -8, -4, 0, 2, 4, 6, 8, 10, 12, 16, 20, 24, 28, 30, 32, 34, 36, 38, 40, 42, 44, 46, 48, 50, 52, 56, 60, 64, 66, 68, 72, 76, 80

^c β sweep, deg: -20, -12, -8, -4, 0, 4, 8, 12, 20 (These numbers represent model α_F .)

Flight calibration of the FADS system consisted of acceleration and deceleration maneuvers, symmetric decelerations to high angles of attack, and sideslip maneuvers at specific angles of attack. For these analyses, multiple maneuvers from several flight days were used. Calibrations were then the best fit of the data. Two acceleration and deceleration maneuvers were flown in phase I of the HARV program to obtain supersonic calibration data. These constant altitude maneuvers began subsonically, accelerated to Mach 1.2, and then decelerated to a set subsonic speed. One maneuver was flown at an altitude of 25,000 ft, and the other was flown at 35,000 ft.

Twenty maneuvers from three flights in phase II were used for the symmetrical decelerations to high angles of attack. These maneuvers consisted of slowly increasing the angle of attack from the trim condition to the desired angle of attack while maintaining 0° sideslip. As the aircraft slowed down, it descended slightly in altitude. Fifteen sideslip maneuvers from two flights in phase II were used to obtain the influence of sideslip on the calibration parameters. These maneuvers consisted of sideslip sweeps at angles of attack from 20° to 65° . The amount of sideslip generated on each maneuver depended on the angle of attack. For angles between 30° and 50° , as much as 15° of sideslip could be obtained in flight.

Calibration parameters $\delta\alpha$, $\delta\beta$, and ϵ were estimated by substituting the reference airdata into the flow model and comparing the model pressure predictions to the pressures that were actually measured. An overdetermined nonlinear least-squares regression was used to determine these calibration parameters. Iterations on the solution were computed until the model-predicted pressures converged to the measured pressures.⁶ The regression was overdetermined because the algorithm was estimating 4 airdata states (α , β , q_c , and p_∞) using 23 independent pressure measurements. The major benefit of the overdetermined system was to make the calibration insensitive to small disturbances in individual pressure measurements. The FADS system works well with as few as nine pressure ports.⁶

Calibration Results From Flight and Wind Tunnel

Calibrations presented here extend previously reported FADS calibrations⁶ to an angle of attack of 70° , to angles of sideslip of $\pm 15^\circ$, and to Mach 1.2. The angle-of-attack calibration parameter is primarily a function of angle of attack.⁶ This parameter is also a function of sideslip angle; therefore, $\delta\alpha$ can be divided into two terms.

$$\delta\alpha = \delta\alpha_{\text{sym}} + \delta\alpha_{\text{asy}}$$

where the symmetric angle-of-attack calibration parameter, $\delta\alpha_{\text{sym}}$, is a function of angle of attack. The asymmetric angle-of-attack calibration parameter, $\delta\alpha_{\text{asy}}$, is a function of angle of sideslip.

The calibration parameter ϵ was represented as a function of Mach number and angle of attack in Ref. 6. However, ϵ is also a function of sideslip; therefore, it can be broken into three terms.

$$\epsilon = \epsilon_M + \epsilon_\alpha + \epsilon_\beta$$

where ϵ_M is a function of Mach number, ϵ_α is a function of angle of attack, and ϵ_β is a function of angle of sideslip.

The calibration parameter $\delta\beta$ was presented as a function of sideslip in Ref. 6. In this analysis, no significant influence of α or M was identified on the $\delta\beta$ calibration parameter. Flight test and wind-tunnel data for each of the terms in the calibration parameters are discussed in the following six subsections.

Effect of Angle of Attack on the Angle-of-Attack Calibration Parameter

The symmetric influence on the angle-of-attack calibration parameter was obtained in subsonic flight from the set of 20 deceleration maneuvers to high angles of attack. Figure 4 shows the results from these maneuvers. The solid line is an empirical curve fit to the individual calibration points from these maneuvers. We determined that this fit best represents the calibration parameter.

Figure 5 shows the root-mean-squared (RMS) error between the flight data and the curve fit as a function of free-stream angle of attack. This RMS error increases with angle of attack but is still within 1° even at an angle of attack of 70° .

Calibrations from wind-tunnel runs 365, 366, and 409 are compared with the flight-determined calibration curve in Fig. 6. Good qualitative agreement occurred between the flight- and wind-tunnel-derived calibration curves with the best agreement at angles of attack from 25° to 50° . Because the wind-tunnel model only consisted of the forebody, this good qualitative agreement demonstrates that the major influence of upwash on $\delta\alpha$ is from the forebody and not the aircraft leading-edge extension and wing. Because upwash can be correlated to the lift coefficient¹⁰, this agreement demonstrates that the lift coefficient generated by the forebody is fairly constant over the low-speed range as would be expected. The usefulness of the wind tunnel in designing a FADS can be clearly seen in this flight-to-wind-tunnel data comparison.

Effect of Sideslip on the Angle-of-Attack Calibration Parameter

Flight and wind-tunnel data were analyzed to determine the influence of sideslip on the angle-of-attack calibration parameter. This analysis was done by subtracting the symmetric term, $\delta\alpha_{sym}$, from the $\delta\alpha$ determined from sideslip data.

$$\delta\alpha_{asy} = \delta\alpha - \delta\alpha_{sym}$$

Calibrations from wind-tunnel runs 428, 430, and 432 show a definite influence of sideslip on the angle-of-attack calibration parameter (Fig. 7). However, the influence is fairly small and does not exceed 1° until sideslips exceed 10° . Note that the effect of sideslip is not symmetrical about $0^\circ \beta$ which may result from slight port alignment errors in the wind-tunnel model.

Also, $\delta\alpha_{asy}$ is slightly affected by angle of attack as can be seen by the curves fanning out at the higher sideslip angles. Flight data were obtained from the set of 15 sideslip maneuvers at different angles of attack. The same parameters used in Fig. 7 were plotted from the flight data and, unlike the wind-tunnel calibration, did not show any systematic influence of sideslip on the angle-of-attack calibration parameter.

Effect of Sideslip on the Angle-of-Sideslip Calibration Parameter

The angle-of-sideslip calibration parameter could be best represented as only a function of sideslip. Flight data were obtained from the 15 sideslip maneuvers at various predetermined angles of attack. Figure 8 shows the flight data with an empirical curve fit. The only effect of angle of attack was a slight change in slope of the angle-of-sideslip calibration parameter curve. This slope change was considered to be a second-order effect and was not modeled in the calibrations for simplicity.

Figure 9 shows the RMS error between the flight-calibration data and the curve fit as a function of free-stream sideslip. The RMS error is approximately 1° for the entire sideslip range. Most of the RMS error resulted from the unmodeled angle-of-attack effects. These flight data are compared with the wind-tunnel data in Fig. 10. The three wind-tunnel runs show identical calibrations for angles of attack between 30° and 36° . Comparing the flight and wind-tunnel calibrations shows that using the wind-tunnel calibration could lead to significant errors in the FADS sideslip estimation. For flight at low sideslip angles, the errors would be on the order of 2° . For higher sideslip angles, the errors could reach 7° .

Effect of Mach Number on the ϵ Calibration Parameter

The calibration parameter ϵ is used in the model to take into account the effects caused by compressibility and high-flow angles. The compressibility effects can be most easily represented as a function of Mach number. For most 1-g high-angles-of-attack and -sideslip flight, the Mach number is relatively low; hence, compressibility effects are not that significant. Therefore, the compressibility effect on ϵ was determined from trimmed data at Mach numbers greater than 0.45. We acknowledge that as Mach number and altitude of the aircraft change, the effective angle of attack determined from the flush ports, α_e , also changes and influences the value of this calibration parameter. For example at Mach 0.45, trimmed α_e at 25,000 ft is 15° lower than trimmed α_e at 35,000 ft. As Mach number increases to 1.2, the difference in α_e for the two altitudes is 2° . The effects of α_e on ϵ_M were found to be secondary for quasi-steady 1-g maneuvering and were not included in the calibration.

Figure 11 presents flight data from two constant-altitude accelerations and decelerations. One maneuver is at an altitude of 25,000 ft, and the other is at 35,000 ft. A flight-calibration curve for ϵ_M obtained from these maneuvers is plotted as the solid line. The value of 0.24 for Mach numbers below 0.45 was extrapolated from the flight data and is shown as a dashed line. Wind-tunnel data are also included from runs 365, 366, and 409. These data are from the ϵ calibration at an effective angle of attack near 0° . These wind-tunnel results seem reasonable when compared to the flight-calibration curve.

Effect of Angle of Attack on the ϵ Calibration Parameter

The calibration parameter ϵ is primarily a function of angle of attack. Figure 12 shows flight data from 20 symmetric maneuvers in which angle of attack was slowly increased. Again, good repeatability is seen in the calibration. The ϵ_α factor is an order of magnitude larger than ϵ_M (Fig. 11) at the higher angles of attack.

Figure 13 shows the RMS error between the calibration data and the curve fit as a function of free-stream angle of attack. The errors increase as angle of attack increases but for the most part remain below 0.10.

Figure 14 shows a comparison between the wind-tunnel and flight data. In this case, the wind-tunnel results agree fairly well with the flight results. These wind-tunnel data basically show no dynamic pressure effects although a slight effect is seen for angles of attack greater than 70° .

Effect of Sideslip on the ϵ Calibration Parameter

The calibration parameter ϵ was expected to be influenced by the angle of sideslip. Figure 15 shows flight results from the 15 sideslip maneuvers. Because these maneuvers were all at low speeds, the influence caused by sideslip was calculated as follows:

$$\epsilon_\beta = \epsilon - \epsilon_\alpha - \epsilon_M = \epsilon - \epsilon_\alpha - 0.24$$

Recall that for low speeds, $\epsilon_M = 0.24$. The magnitude of the ϵ_β term is fairly small when compared with the ϵ_α term. Note that the ϵ_β parameter is not symmetrical about $\beta_e = 0$. This asymmetry could be attributed to a slight misalignment of the FADS ports on the HARV.

The RMS error between the curve fit in Fig. 15 and the flight data is shown in Fig. 16 as a function of free-stream angle of sideslip. Again, the RMS error is basically less than 0.10.

Figure 17 compares the flight and wind-tunnel data. This comparison is fair for sideslip angles between $\pm 10^\circ$ and poor for sideslip angles less than -10° and greater

than 10° . The wind-tunnel data show a symmetrical calibration about $\beta_e = 0$.

Airdata Estimation Using the Calibrated Flush Airdata Sensor

Of course, the real test of the calibrations is how well they can be used in the FADS algorithm to determine the free-stream airdata quantities. Again, note that the calibrations presented were for quasi-steady flight conditions, and they are not expected to represent highly dynamic flight. The FADS algorithm was previously described in detail.⁶

The following subsections describe the ability of the FADS algorithm to accurately obtain airdata from flight-measured pressures. The first subsection presents the FADS algorithm using the flight-derived calibrations. The second subsection presents the FADS algorithm using the wind-tunnel-derived calibrations. Comparisons are made between the results from the flight-derived calibrations and the wind-tunnel-derived calibrations.

Airdata Estimation Using Flight-Derived Calibrations

Two maneuvers that were not used in the calibrations were chosen to demonstrate the effectiveness of the FADS algorithm in determining the free-stream airdata. The first is one of the few supersonic test points flown in the HARV program. The second is of a high-angle-of-attack maneuver with large sideslip sweeps. Figures 18 and 19 show time histories for these maneuvers. The reference airdata shown in Figs. 18 and 19 were obtained from the calibrated wingtip airdata sensors on the HARV.

The first demonstration maneuver (Fig. 18) was picked from a group of dynamic maneuvers at supersonic speeds. This maneuver was flown in phase I of the HARV program; thus, the aircraft was not augmented with thrust vectoring. Unlike the calibration maneuvers, portions of this maneuver were very dynamic. The FADS airdata estimations were, therefore, not expected to be very accurate during those portions of the maneuver. Figure 18(a) shows the Euler angle and Mach number time histories. From this figure, the dynamic portions of the maneuver can be identified. Because this maneuver was very dynamic, the wingtip airdata probe measurements were blended with inertial data to determine an enhanced airdata reference.¹¹

The reference Mach number and the FADS-estimated Mach number are shown in Fig. 18(b) for this maneuver. The difference between these two values represents the error in the FADS Mach number estimation. The supersonic portion of the maneuver is

specifically identified with shading. Mach number error was within 0.04 throughout the maneuver. For the 1-g, low-rate portion of this maneuver (the first 70 sec), the Mach error was basically within 0.01 with a slight deviation as the aircraft passed through Mach 1.

Figure 18(c) shows the pressure-altitude time histories. For the low-rate portions of the maneuver, the FADS pressure-altitude errors are basically within 500 ft. The largest errors occurred during the loaded high-rate portions of the maneuver.

Figure 18(d) shows the angle-of-attack time histories. Nearly 45° of angle of attack were used in this maneuver to rapidly change the aircraft-heading angle. The FADS angle-of-attack error remained below 1° for the low-rate portions of the maneuver. The error remained below 4° for the highly dynamic portions of the maneuver. These low errors demonstrate that the symmetric angle-of-attack calibration parameter holds well for high-speed, loaded flight conditions even though the calibrations were derived exclusively from low-speed, 1-g flight.

Figure 18(e) shows the angle-of-sideslip time histories. For the low-rate portions of the maneuver, the errors remained below 1°. For the high-rate portions, errors remained below 3°. The larger errors seen in the dynamic portions of the maneuver suggest that future work needs be done to account for dynamic effects in the FADS algorithm.

The second demonstration maneuver (Fig. 19) contained a constant altitude deceleration from Mach 0.7 to an angle of attack of 65°. Then the maneuver continued with sideslip sweeps at angles of attack of 60°, 50°, 40°, and 30° while descending from 29,000 to 14,000 ft. Figure 19(a) shows the angle-of-attack time history. The difference between the reference angle of attack and the FADS-estimated angle of attack is also plotted. The FADS-estimated angle of attack agrees very well with the reference angle of attack throughout the angle-of-attack range. For the no sideslip deceleration, the errors remained below 1°. The largest errors were observed during the large sideslip excursions (Fig. 19(b)). These larger errors resulted from the dynamics of the maneuver and from not having a flight-determined calibration for the influence of sideslip on the angle-of-attack calibration parameter.

Figure 19(b) shows the angle of sideslip time history. This time history shows fairly good agreement between the reference and the FADS signal for angles of sideslip approaching 20°.

The Mach number time histories (Fig. 19(c)) show excellent agreement for the high-angle-of-attack portion of the maneuver and good agreement for the deceleration to high angles of attack. For the

high-angle-of-attack portion, Mach number errors are approximately within ± 0.005 .

Figure 19(d) shows the FADS pressure-altitude estimation is in good agreement with the reference pressure altitude throughout the maneuver. The best agreement is in the high-angle-of-attack portion of the maneuver where the errors are less than 100 ft.

Airdata Estimation Using Wind-Tunnel-Derived Calibrations

The wind-tunnel-derived calibrations were installed in the FADS algorithm to determine the FADS airdata estimation using only wind-tunnel calibrations. Running the algorithm on flight data demonstrates the accuracy of a FADS system that was not calibrated with an extensive flight-calibration program. The second demonstration maneuver will be used because the wind-tunnel calibrations were obtained at low speeds. Figure 20 shows the results from applying the wind-tunnel calibrations to the flight data.

Figure 20(a) shows a time history of angle of attack computed using the flight calibration and angle of attack computed using the wind-tunnel calibration. The difference between the two computations is also plotted. The largest difference is at the highest angle-of-attack condition. For angles of attack below 50°, the wind-tunnel-based algorithm gave angles of attack within 2° of the angles of attack determined from the flight-based algorithm. Above an angle of attack of 50°, the errors were still within 6°.

Figure 20(b) shows the angle-of-sideslip time histories. An offset of nearly 2° exists at the low sideslip conditions. For the sideslip sweeps, the error remained below $\pm 5^\circ$.

Figure 20(c) shows the Mach number time histories. The Mach number determined from the wind-tunnel calibrations is consistently lower than that determined using the flight calibrations. This error diminishes as the speed decreases with increasing angle of attack. At low-speed conditions, the Mach number error remains below 0.02. It makes sense that the wind-tunnel calibrations would estimate Mach number better at the low-speed conditions. Because only low-speed wind-tunnel data were available, obtaining an ϵ_M which takes into account compressibility effects was not possible. Hence at the higher speeds, the Mach number estimation is expected to be lower than the true Mach number.

Figure 20(d) shows the pressure-altitude time histories. Inability to obtain compressibility effects in the wind-tunnel-derived calibrations caused the pressure-altitude estimate to be lower than that derived using flight calibrations. The error varied from 800 ft at high

speeds (low angle of attack) to approximately 100 ft at low speeds (high angle of attack).

Concluding Remarks

This report presented flight and wind-tunnel calibrations of a nonintrusive airdata sensor and then assessed the applicability of the wind tunnel for sensor design and calibration. Flight calibrations of an F-18 nosetip-mounted flush airdata sensor (FADS) were obtained for 1-g quasi-steady flight to an angle of attack of 70° , to angles of sideslip of $\pm 15^\circ$, and to Mach 1.2. Low-speed, wind-tunnel calibrations of an identical FADS on a full-scale F-18 forebody were also obtained for angles of attack to 80° and angles of sideslip to nearly $\pm 20^\circ$. Data from 23 FADS pressure ports were related to the airdata parameters through a mathematical model.

The mathematical model was based on low-speed potential flow theory and adjusted empirically from flight calibrations. When the FADS algorithm was applied to flight data, this model worked well without extension into the low supersonic flight regime and into the high-flow-angle regimes. The largest errors occurred in the highly dynamic portions of the maneuvers. This result suggests that future work needs to be done to account for the dynamic effects in the FADS algorithm.

A major emphasis of this research was to demonstrate the usefulness of the wind tunnel in preliminary design and calibration of FADS systems. From the wind tunnel, the designer can determine the sensitivity of the FADS calibration parameters to angles of attack and sideslip and to airspeed and thus avert an extensive flight-calibration program. Low-speed, wind-tunnel calibrations of the FADS showed good qualitative agreement with the flight-derived calibrations. This agreement suggested that using the wind-tunnel-derived calibrations in the FADS algorithm would yield reasonable estimates of flight-airdata quantities. When applied to flight data, the accuracies of the FADS algorithm with the low-speed, wind-tunnel calibrations were shown. Mach number and altitude estimates were best at low-speeds. This result was expected because only low-speed, wind-tunnel data were available, and these two parameters are significantly affected by compressibility. The angle-of-attack and -sideslip estimates were within 5° for all flow angles and were better at the lower flow angles.

Use of the wind tunnel as a design tool for FADS development still needs further investigation. For example, a significant issue is scaling effects. The designer will typically not have the luxury of a full-scale model, especially for higher speed wind-tunnel tests. In

addition, the nose of the aircraft may not always be the best location for the FADS system; therefore, the wind tunnel could be very beneficial in the design and development of off-nose FADS systems.

References

- ¹Jane's *All the World's Aircraft*, 81st Ed., 1990-91, pp. 473.
- ²Wolowicz, Chester H. and Terrence D. Gossett, *Operational and Performance Characteristics of the X-15 Spherical, Hypersonic Flow-Direction Sensor*, NASA TN D-3070, 1965.
- ³Siemers, P.M. III, H. Wolf, and M.W. Henry, "Shuttle Entry Air Data System (SEADS)—Flight Verification of an Advanced Air Data System Concept," AIAA 88-2104, May 1988.
- ⁴Burnette, Jamie B., Richard F. Hellbaum, and H. Douglas Garner, *A Proposed Computational Technique for Obtaining Hypersonic Air Data on a Sharp-Nosed Vehicle*, NASP CR-1066, Nov. 1989.
- ⁵Fisher, David F., David M. Richwine, and Daniel W. Banks, *Surface Flow Visualization of Separated Flows on the Forebody of an F-18 Aircraft and Wind-Tunnel Model*, NASA TM-100436, 1988.
- ⁶Whitmore, Stephen A., Timothy R. Moes, and Terry J. Larson, *Preliminary Results From a Subsonic High Angle-of-Attack Flush Airdata Sensing (HI-FADS) System: Design, Calibration, and Flight Test Evaluation*, NASA TM-101713, 1990.
- ⁷Regenie, Victoria, Donald Gatlin, Robert Kempe, and Neil Matheny, "The F-18 High Alpha Research Vehicle: A High-Angle-of-Attack Testbed Aircraft," AIAA-92-4120, Aug. 1992. (Also available as NASA TM-104253, 1992.)
- ⁸DeFrance, Smith J., *The N.A.C.A. Full-Scale Wind Tunnel*, NACA TR-459, 1933.
- ⁹Moes, Timothy R. and Stephen A. Whitmore, *A Preliminary Look at Techniques Used to Obtain Airdata From Flight at High Angles of Attack*, NASA TM-101729, 1990.
- ¹⁰Kuethe, Arnold M. and Chuen-Yen Chow, *Foundations of Aerodynamics: Bases of Aerodynamic Design*, 4th Ed., Wiley & Sons, New York, 1986, pp. 80-81.
- ¹¹Moes, Timothy R. and Stephen A. Whitmore, "Preliminary Results From an Airdata Enhancement Algorithm With Application to High Angle-of-Attack Flight," AIAA 91-0672, Jan. 1991. (Also available as NASA TM-101737, 1991.)

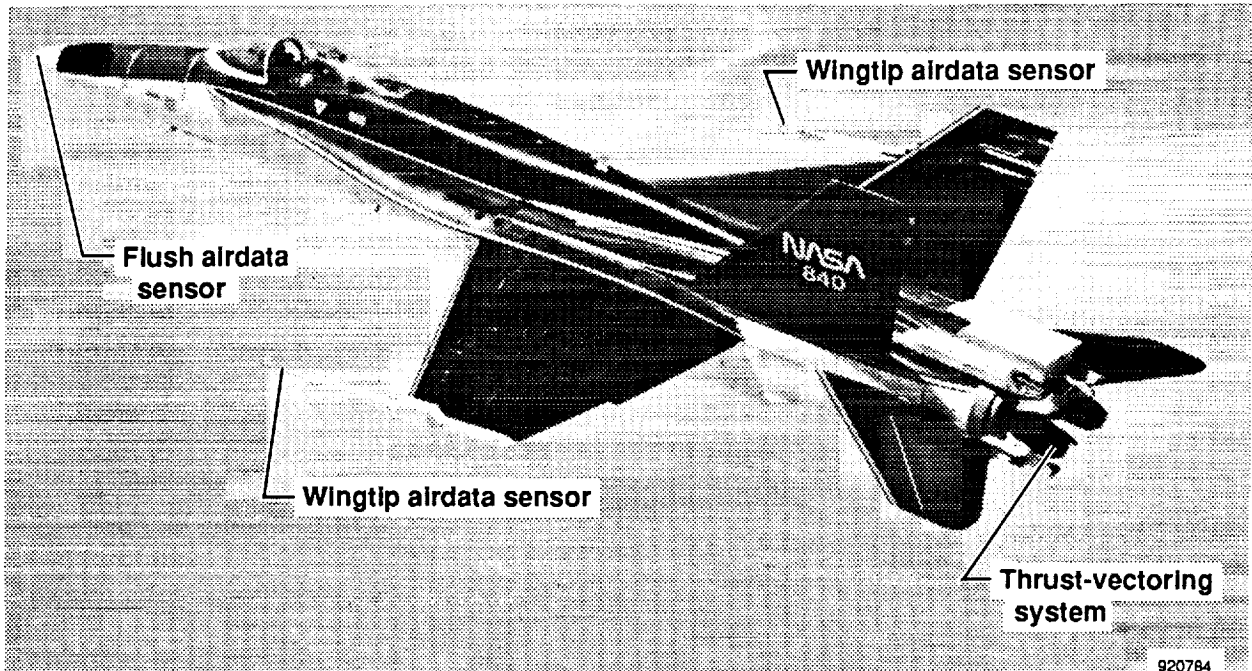


Fig. 1 The F-18 High Alpha Research Vehicle.

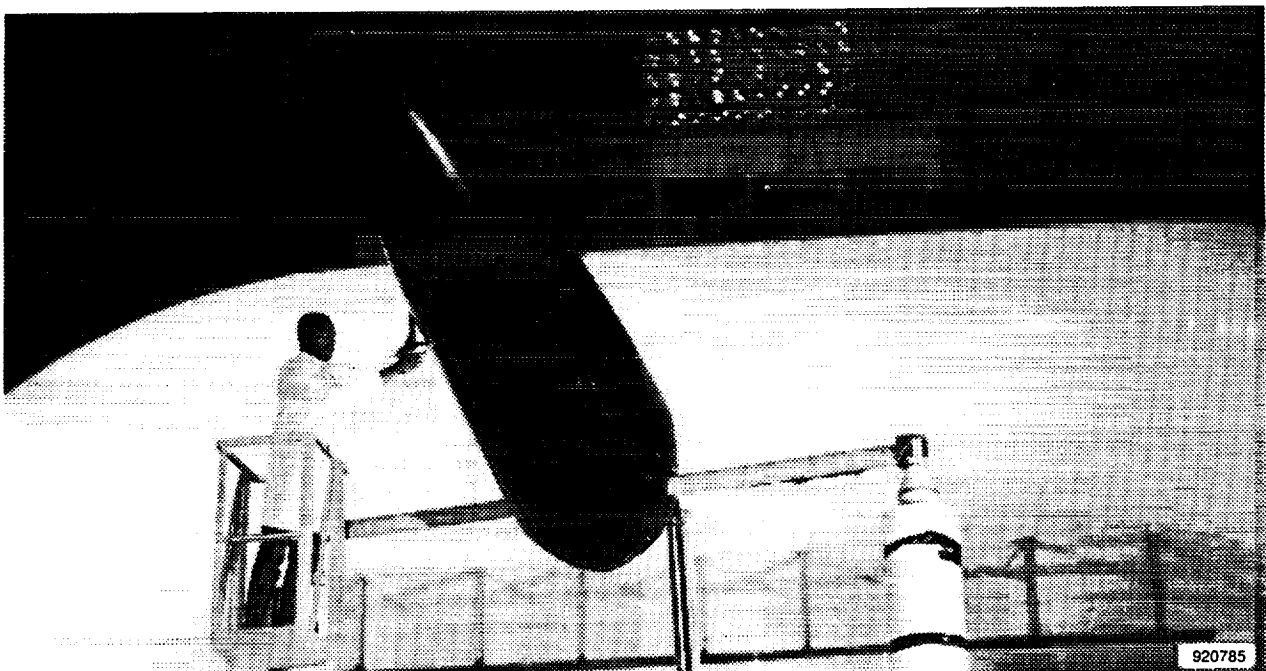


Fig. 2 Full-scale F-18 forebody installed in the Langley 30- by 60-Foot Wind Tunnel.

ORIGINAL PAGE
BLACK AND WHITE PHOTOGRAPH

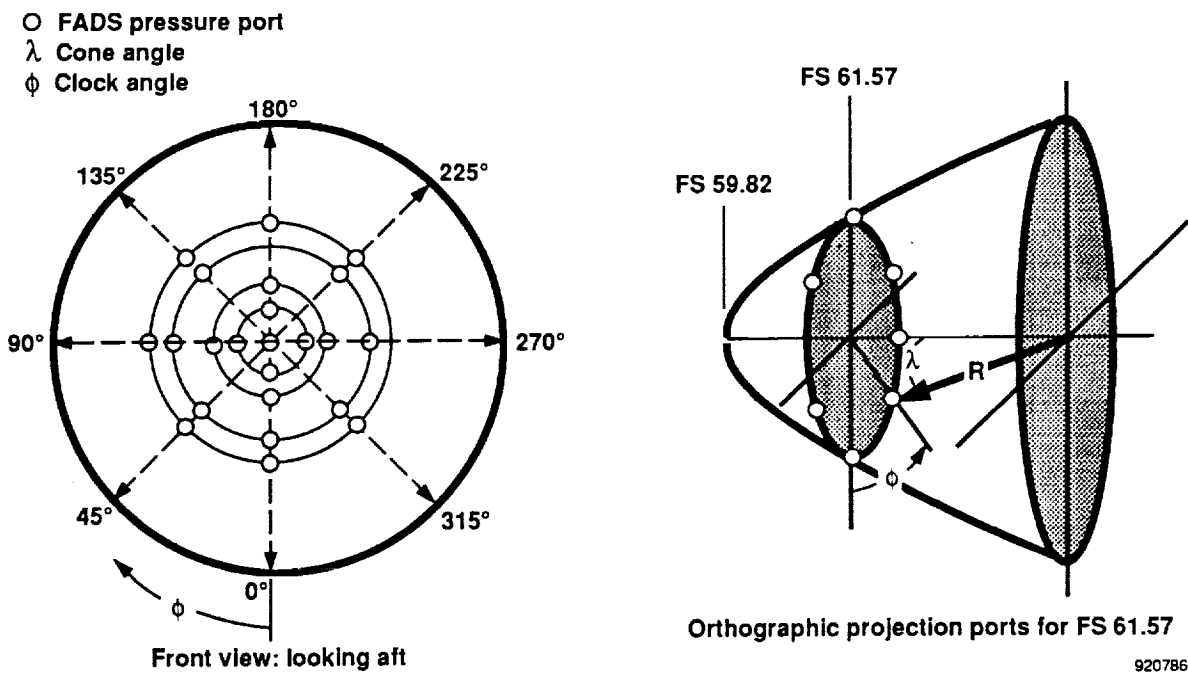


Fig. 3 The flush airdata sensor nose cap showing coordinate definitions and port locations.

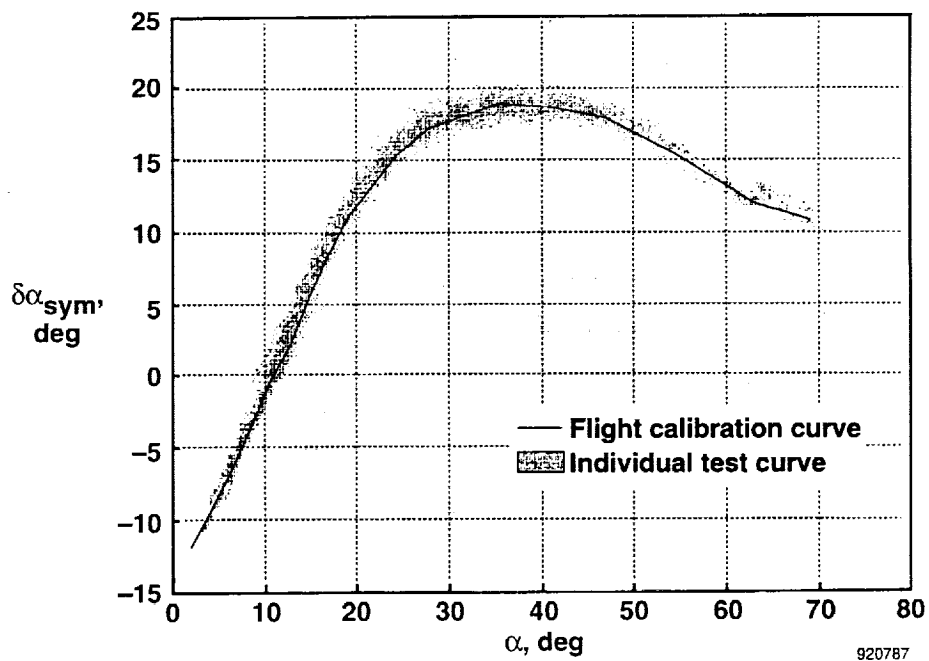


Fig. 4 Flight results for the symmetric angle-of-attack calibration parameter.

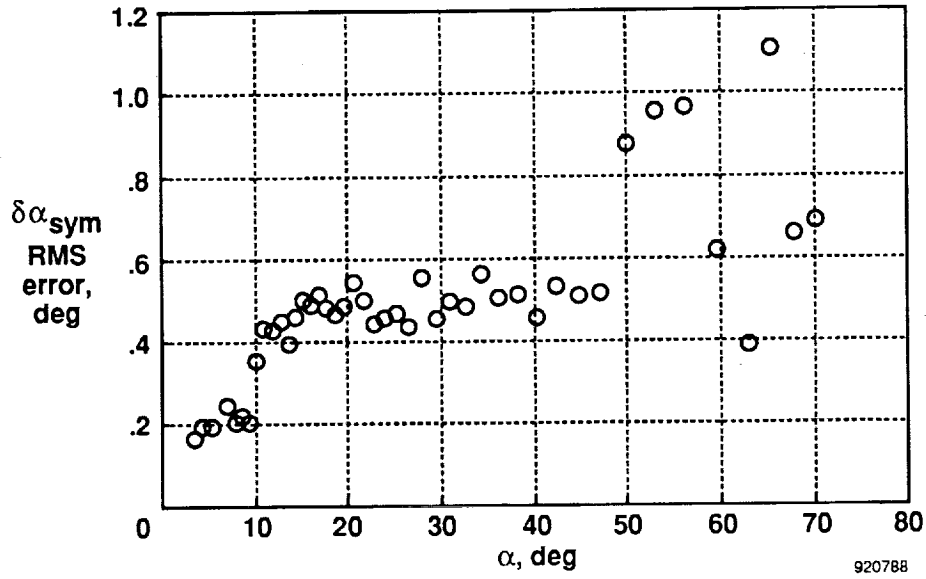


Fig. 5 Symmetric angle-of-attack calibration parameter root-mean-squared error between the flight-calibration curve and the actual test points

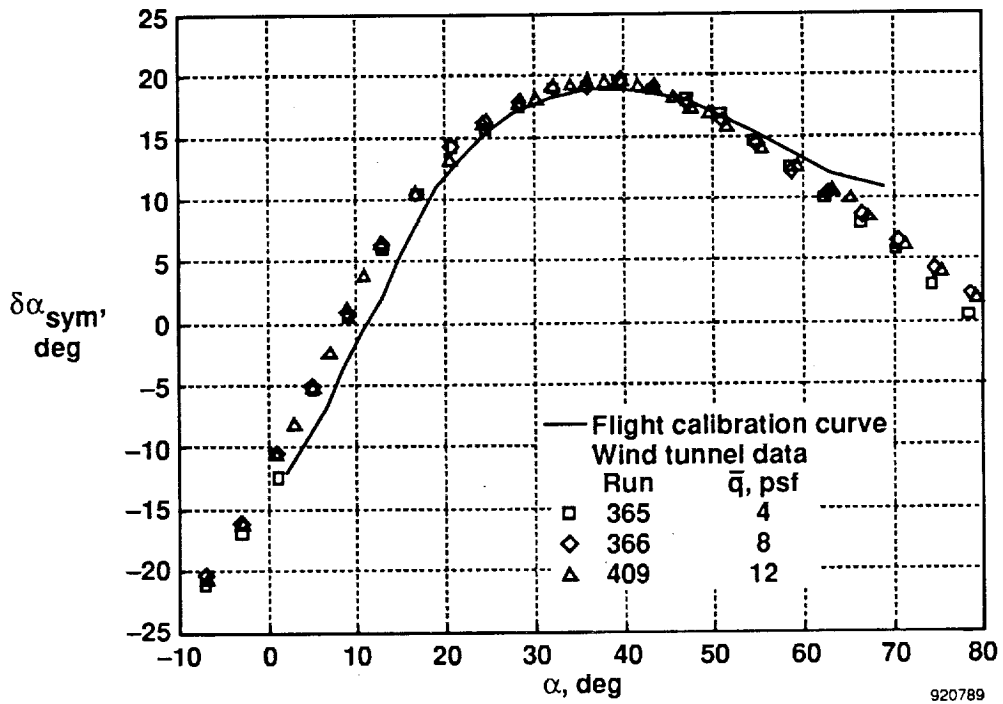


Fig. 6 Flight- and wind-tunnel-derived symmetric angle-of-attack calibration parameter.

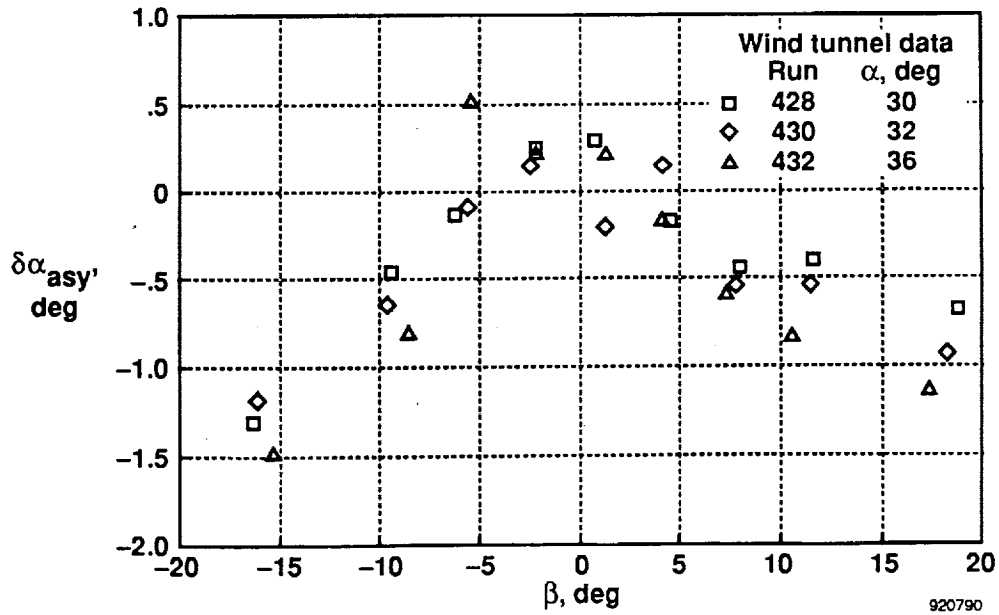


Fig. 7 Asymmetric angle-of-attack calibration parameter determined from wind-tunnel data.

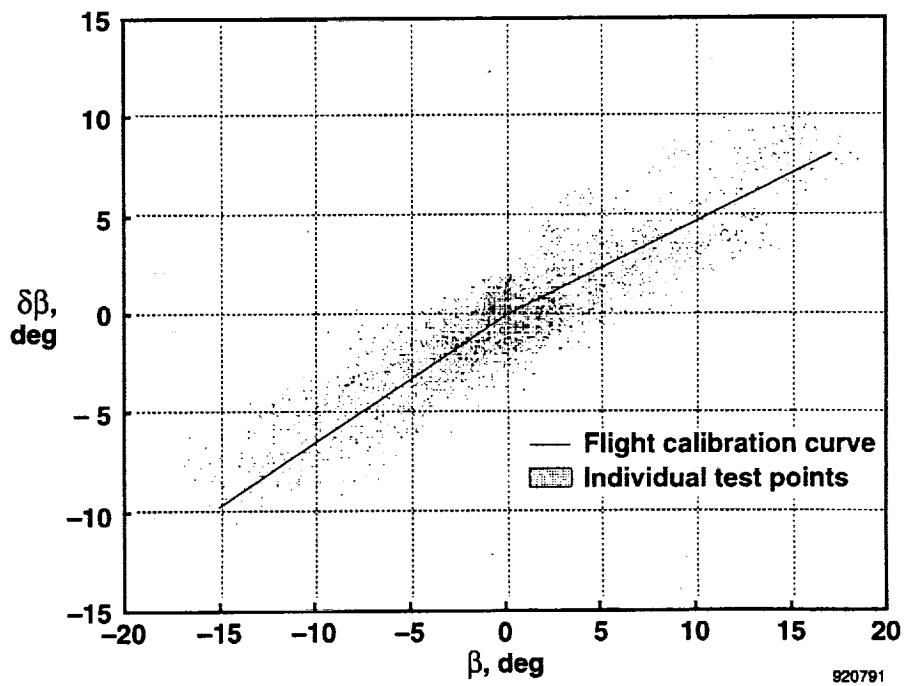
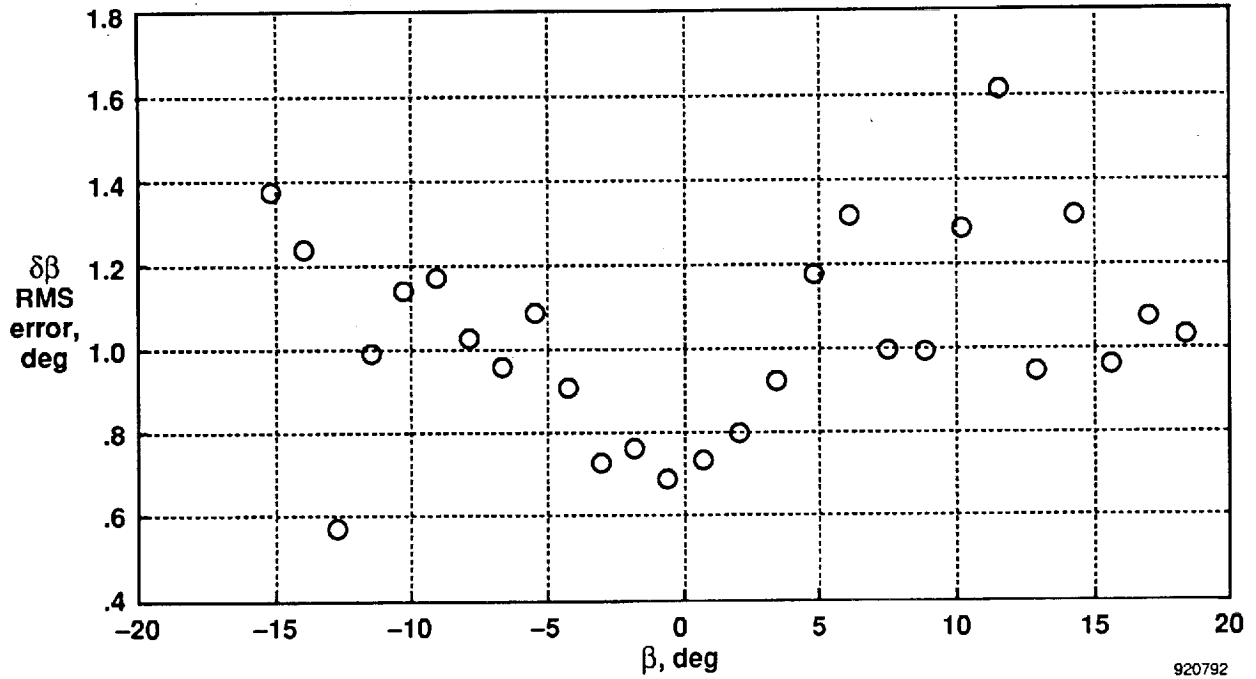
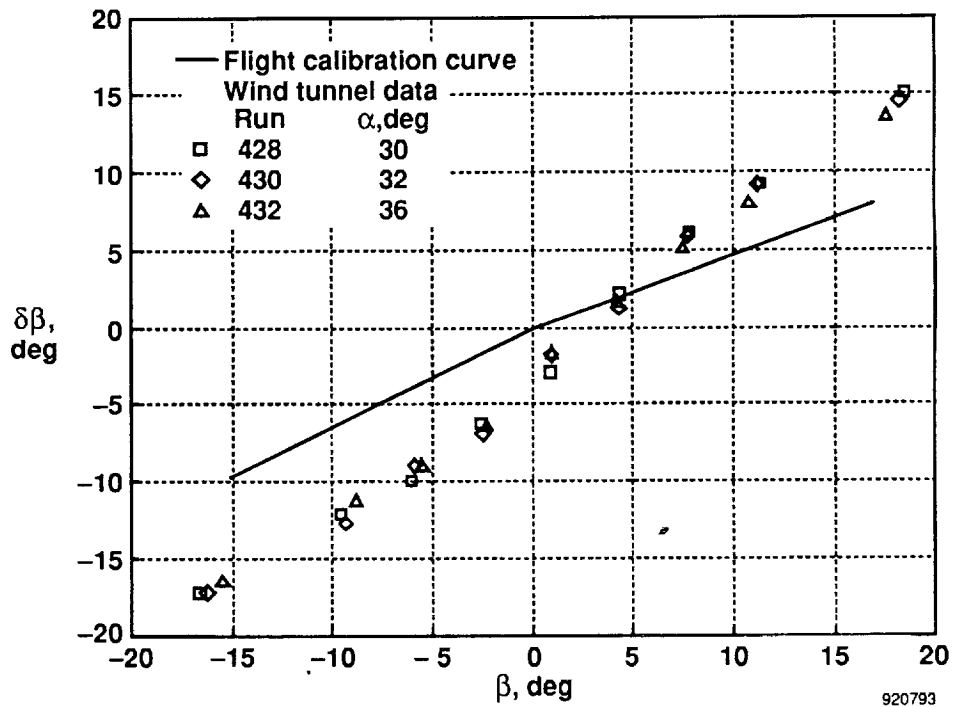


Fig. 8 Flight results for the angle-of-sideslip calibration parameter.



920792

Fig. 9 Angle-of-sideslip calibration parameter root-mean-squared error between the flight-calibration curve and the actual test points.



920793

Fig. 10 Flight- and wind-tunnel-derived angle-of-sideslip calibration parameter.

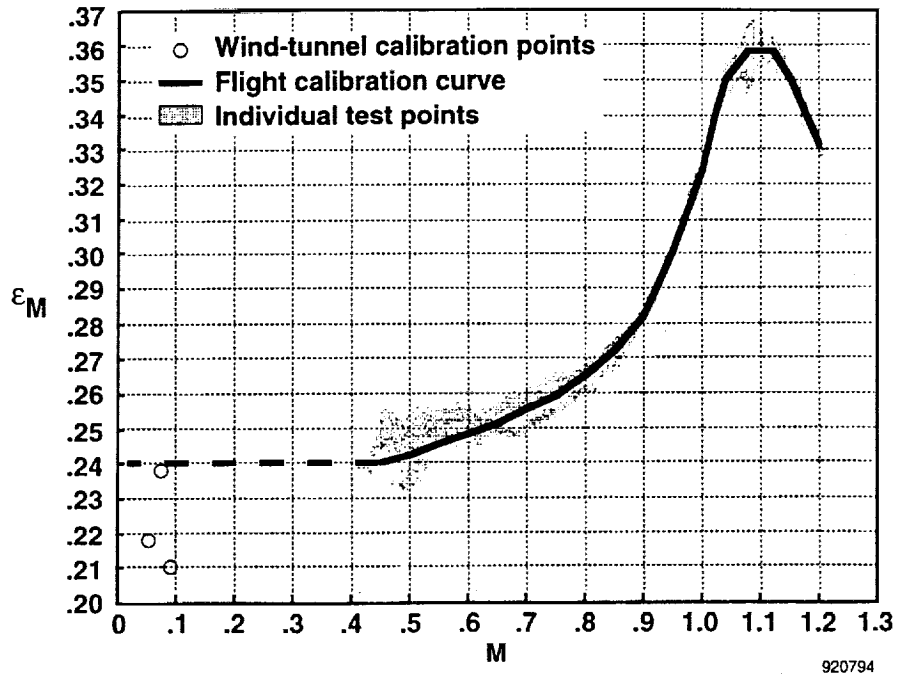


Fig. 11 Flight and wind-tunnel calibration results for the ϵ_M calibration parameter.

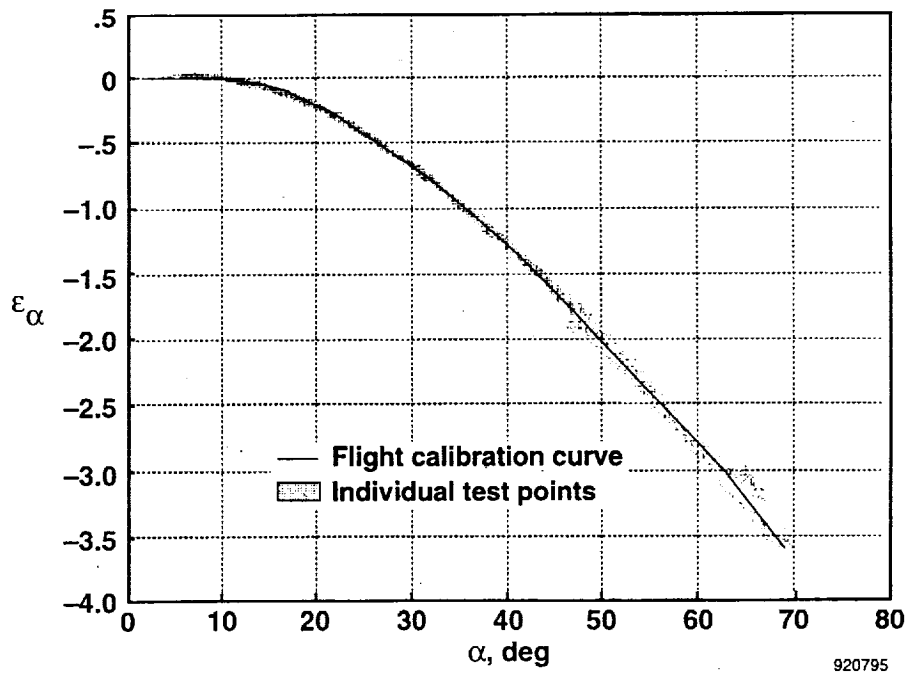


Fig. 12 Flight results for the ϵ_α calibration parameter.

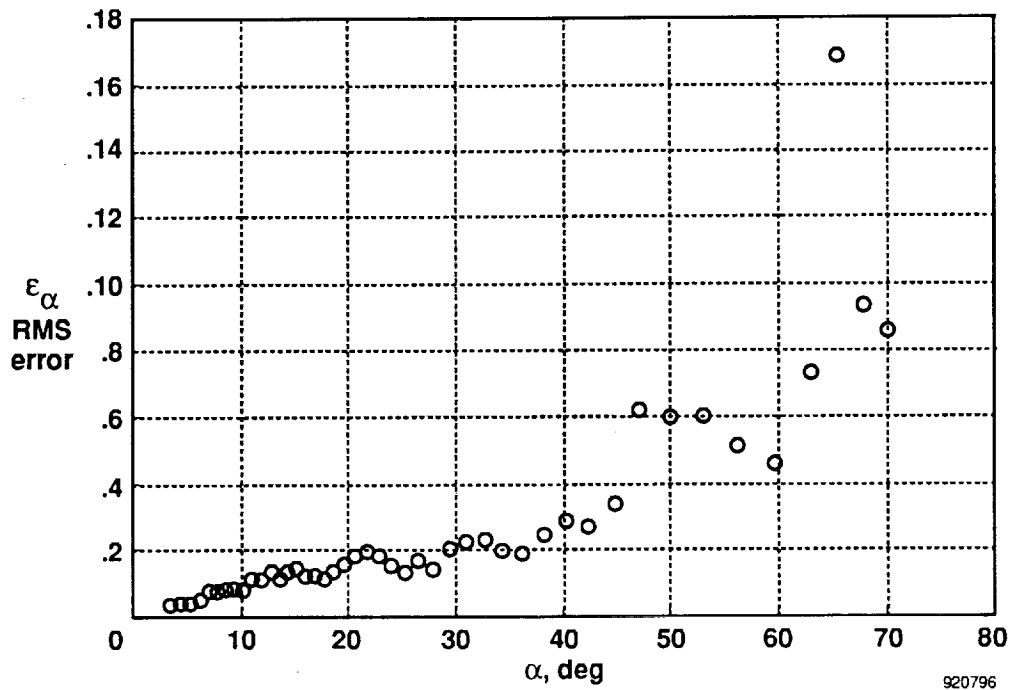


Fig. 13 Root-mean-squared error between the flight-calibration curve and the actual test points for the ϵ_α calibration parameter.

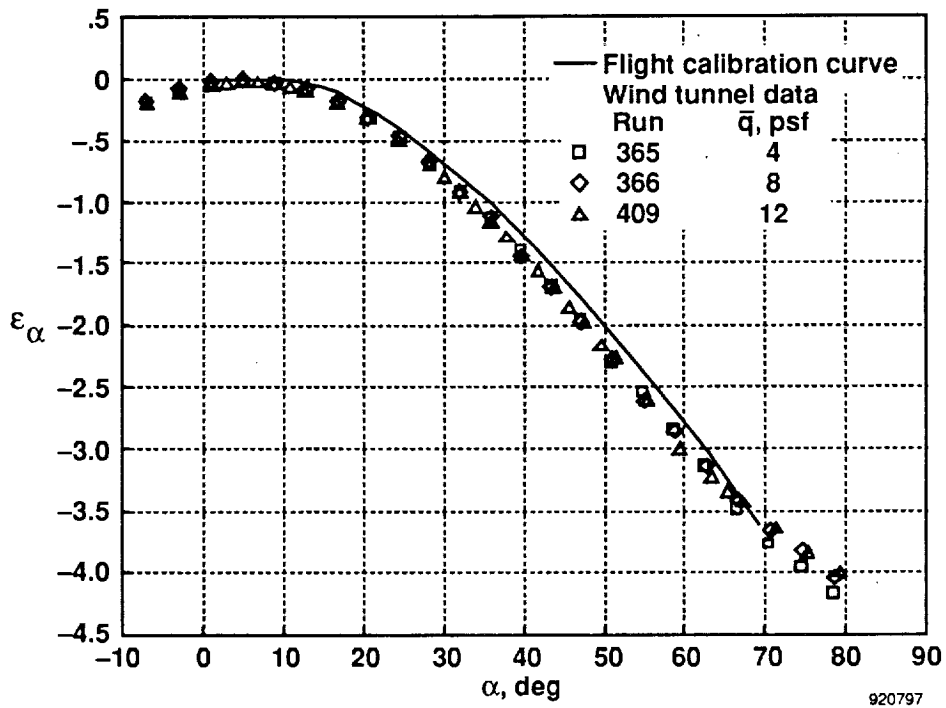


Fig. 14 Flight and wind-tunnel-derived ϵ_α calibration parameter.

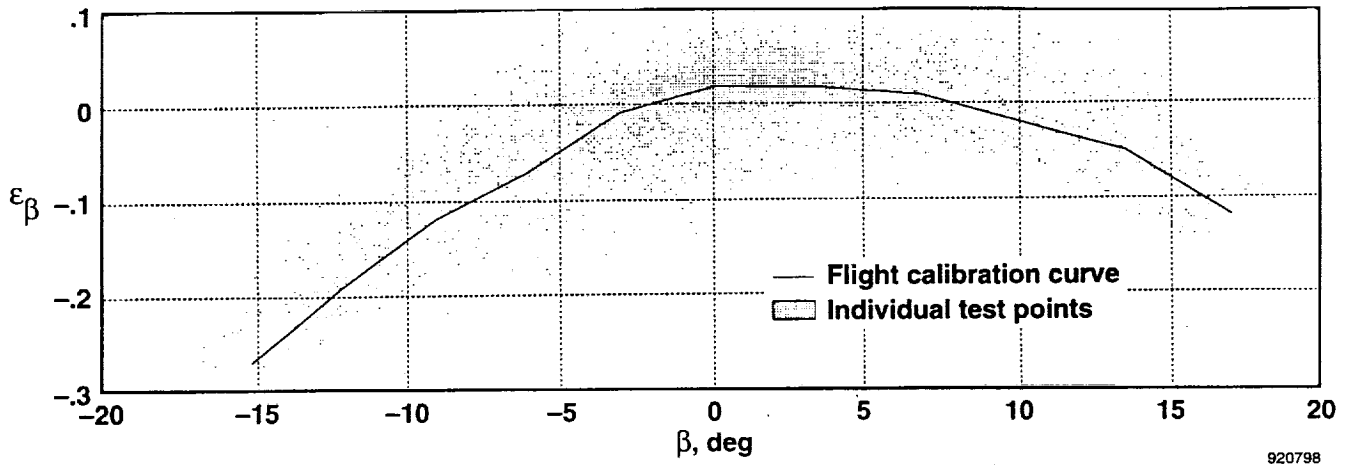


Fig. 15 Flight results for the ϵ_β calibration parameter.

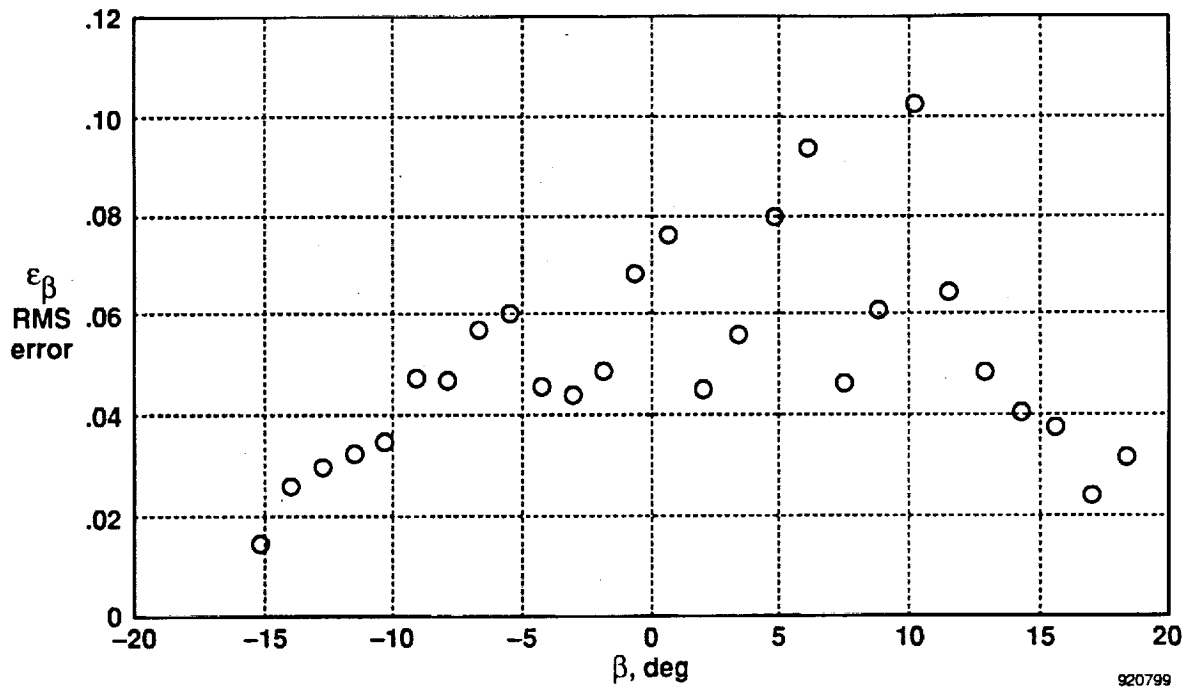


Fig. 16. Root-mean-squared error between the flight-calibration curve and the actual test points for the ϵ_β calibration parameter.

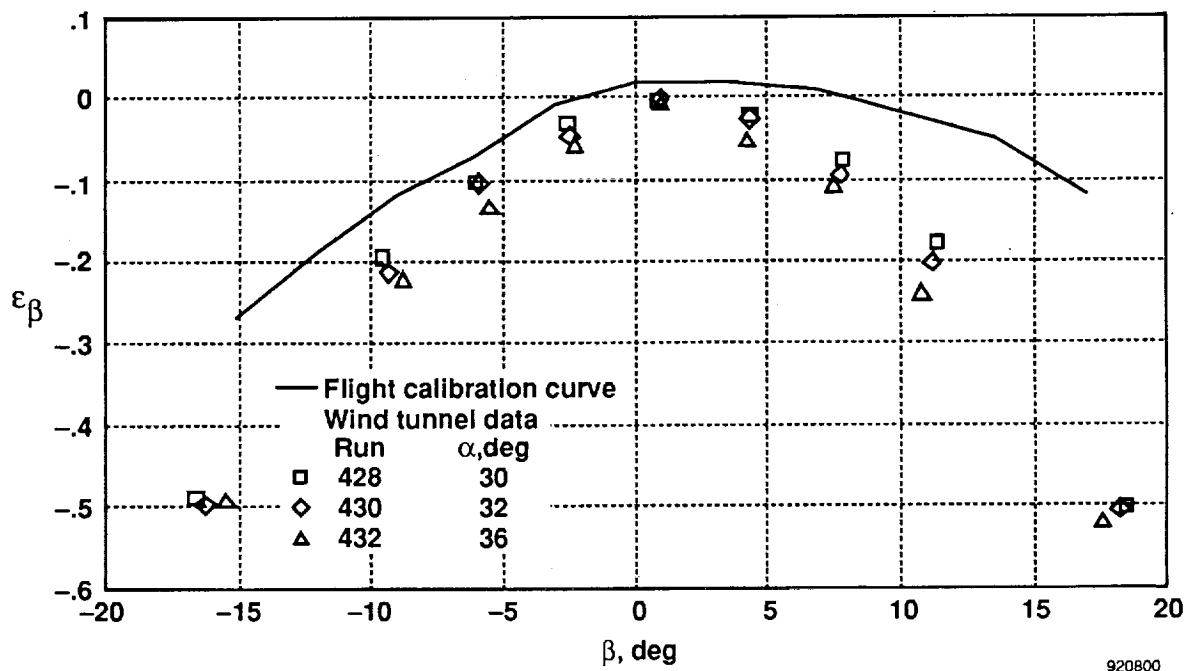
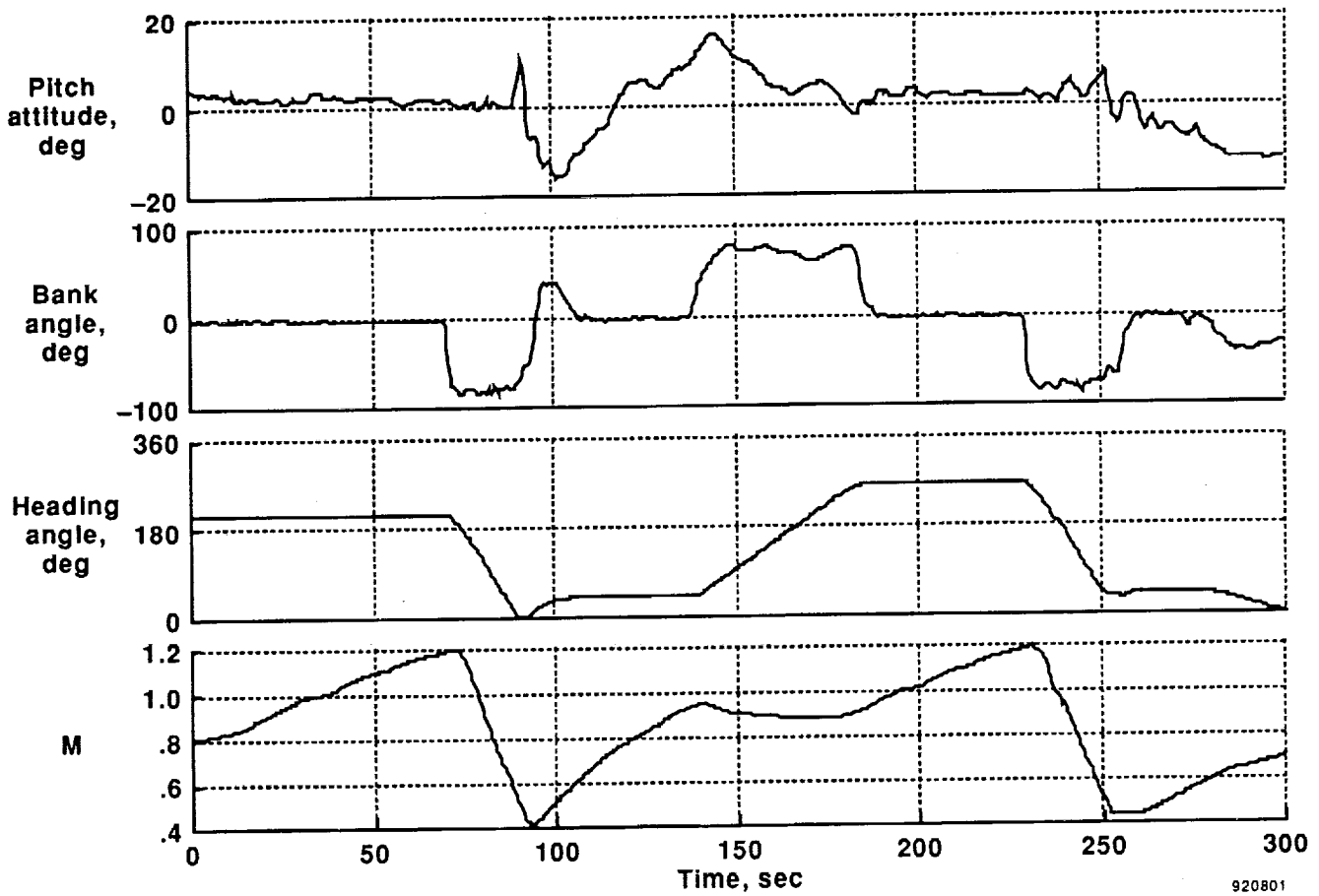
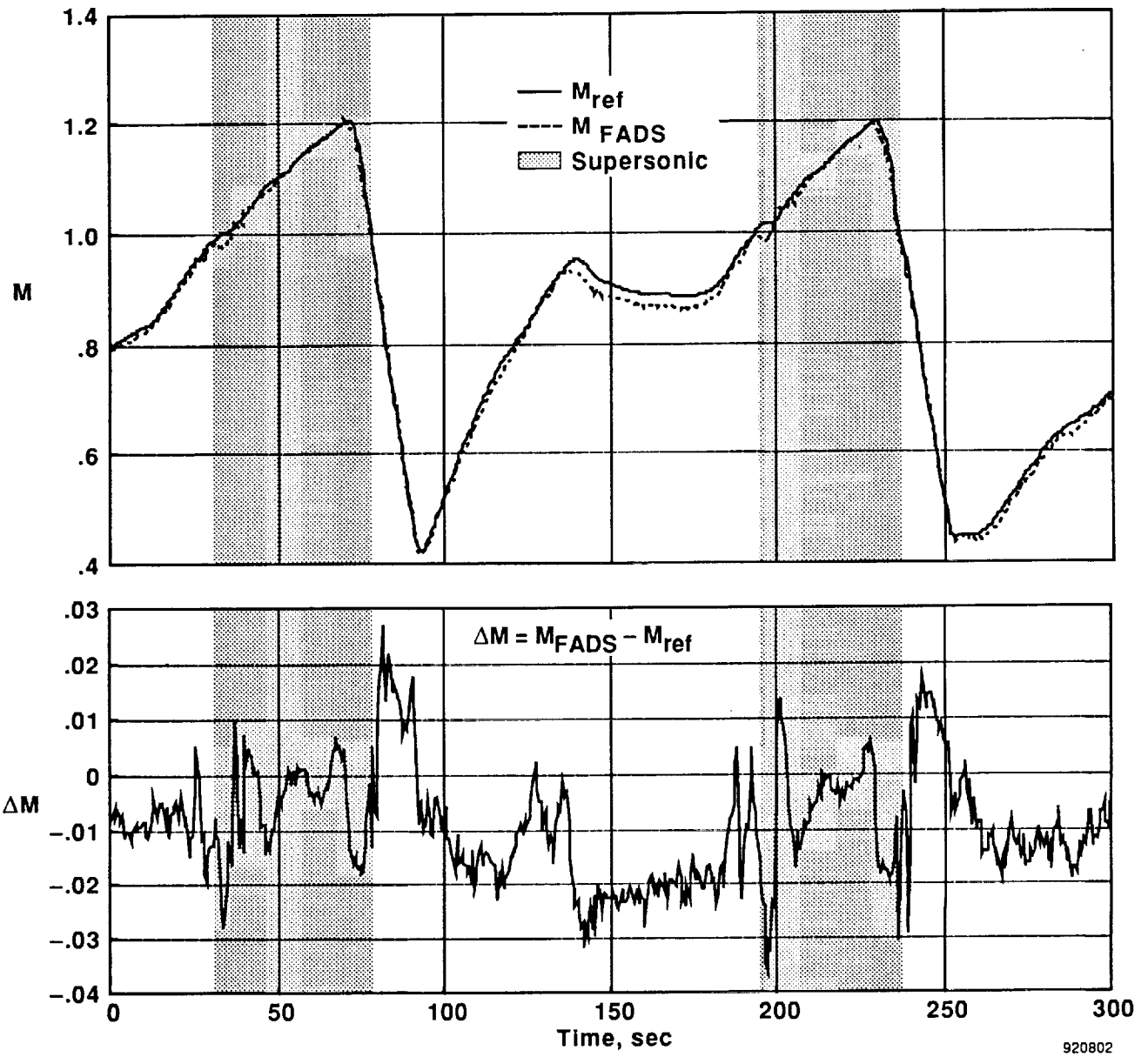


Fig. 17 Flight- and wind-tunnel-derived ϵ_{β} calibration parameter.



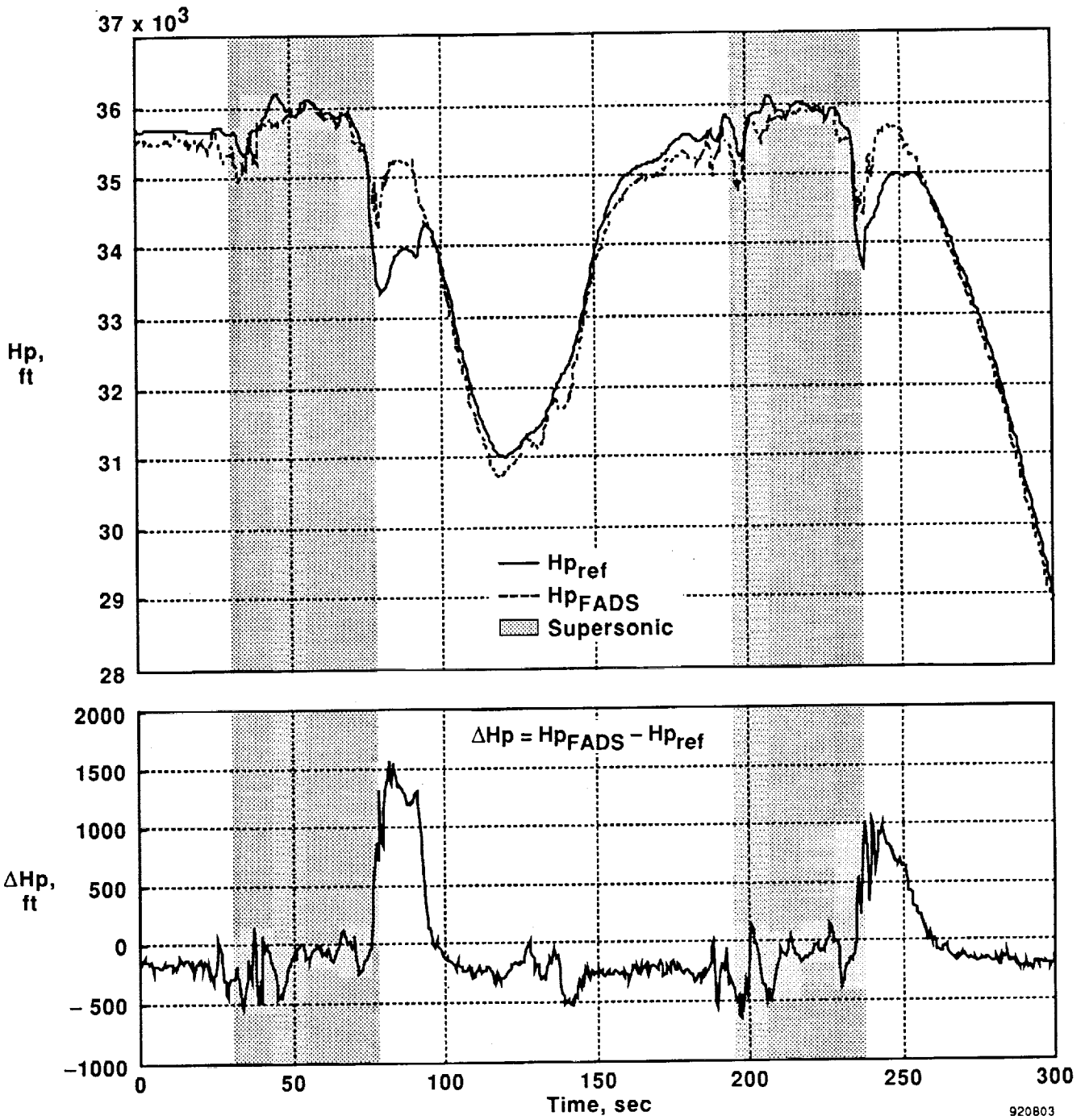
(a) Euler angles and Mach number.

Fig. 18 Time histories for the high-speed maneuver.

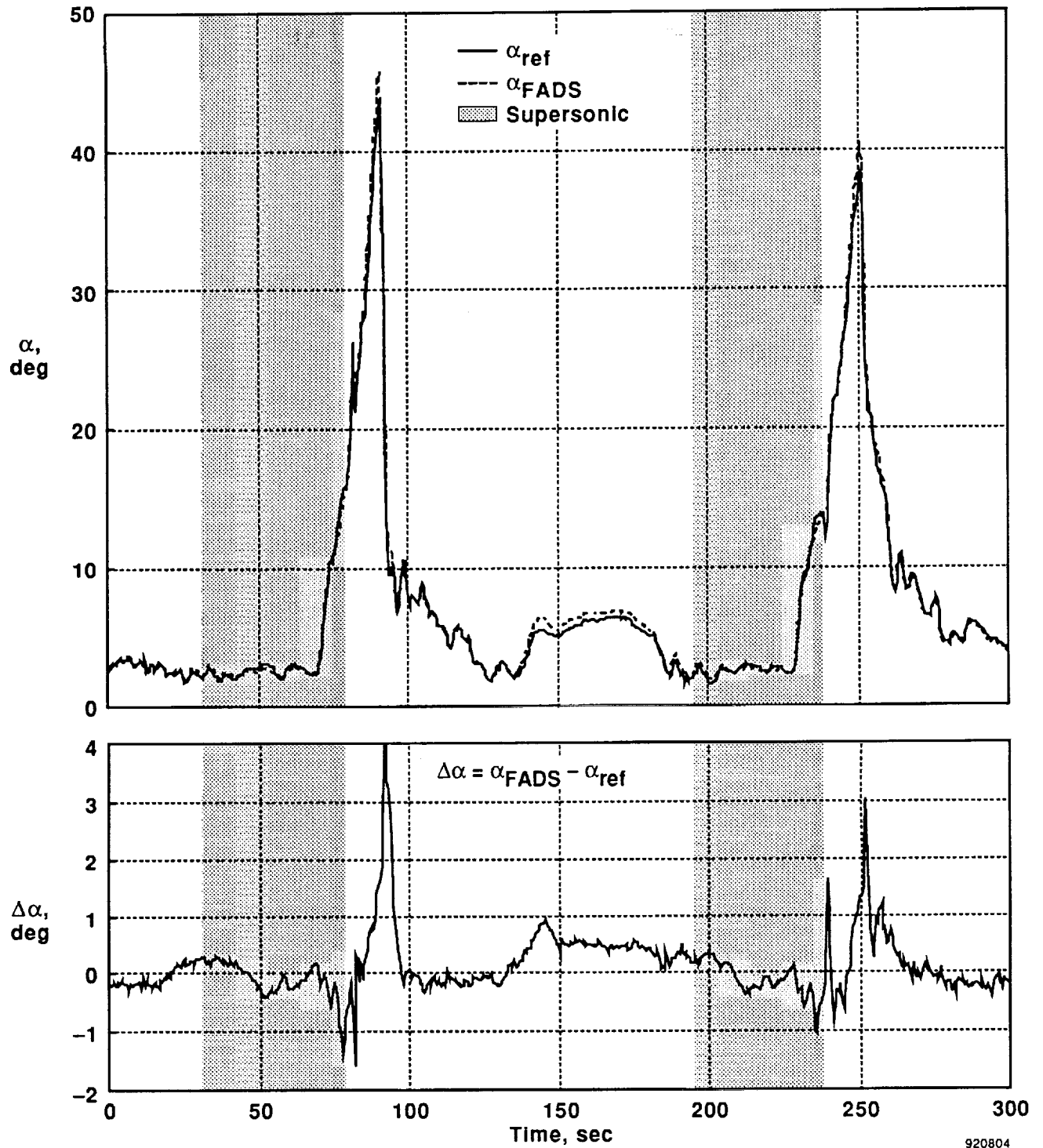


920802

(b) Mach number.
 Fig. 18 Continued.

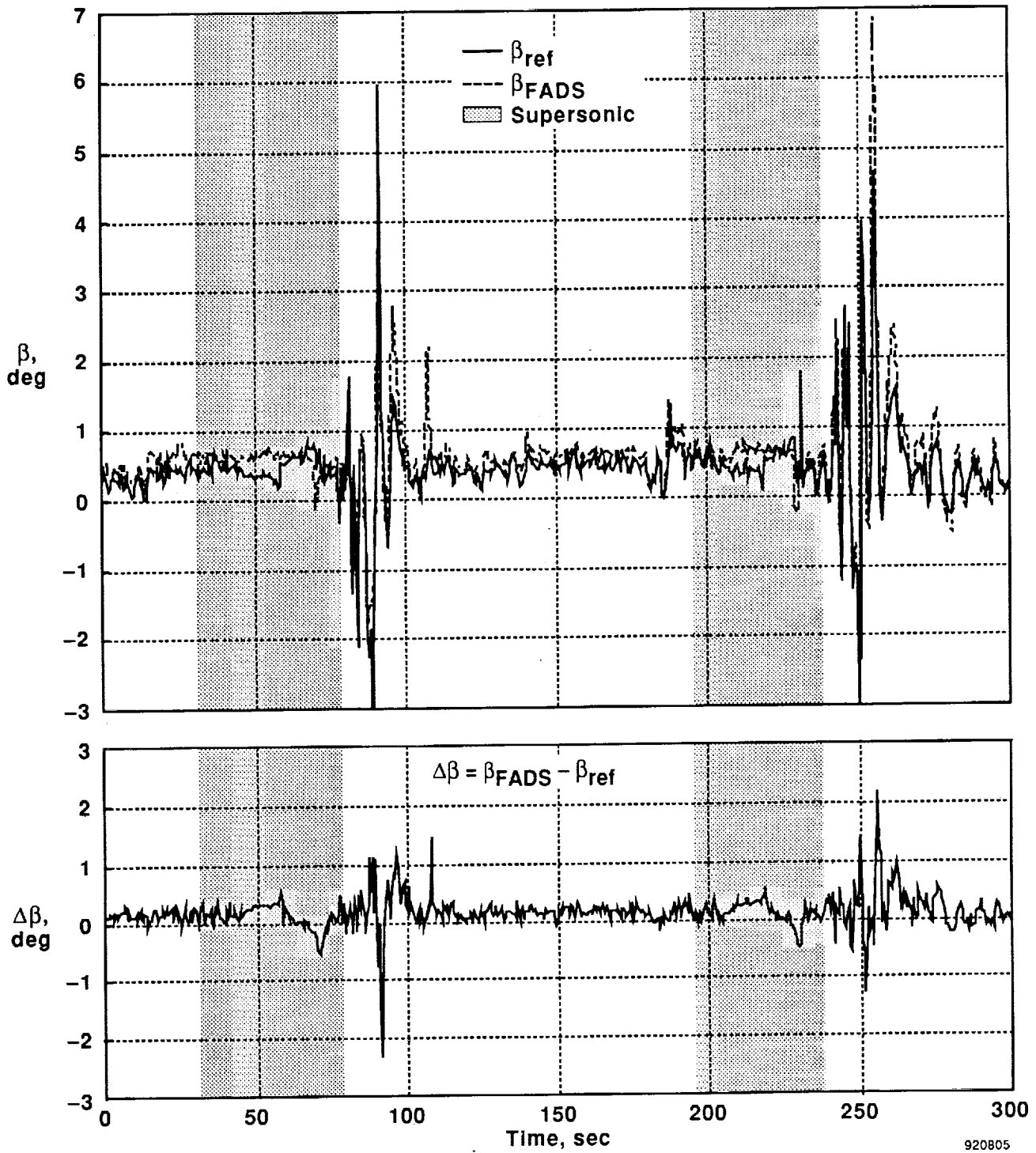


(c) Pressure altitude.
 Fig. 18 Continued.



920804

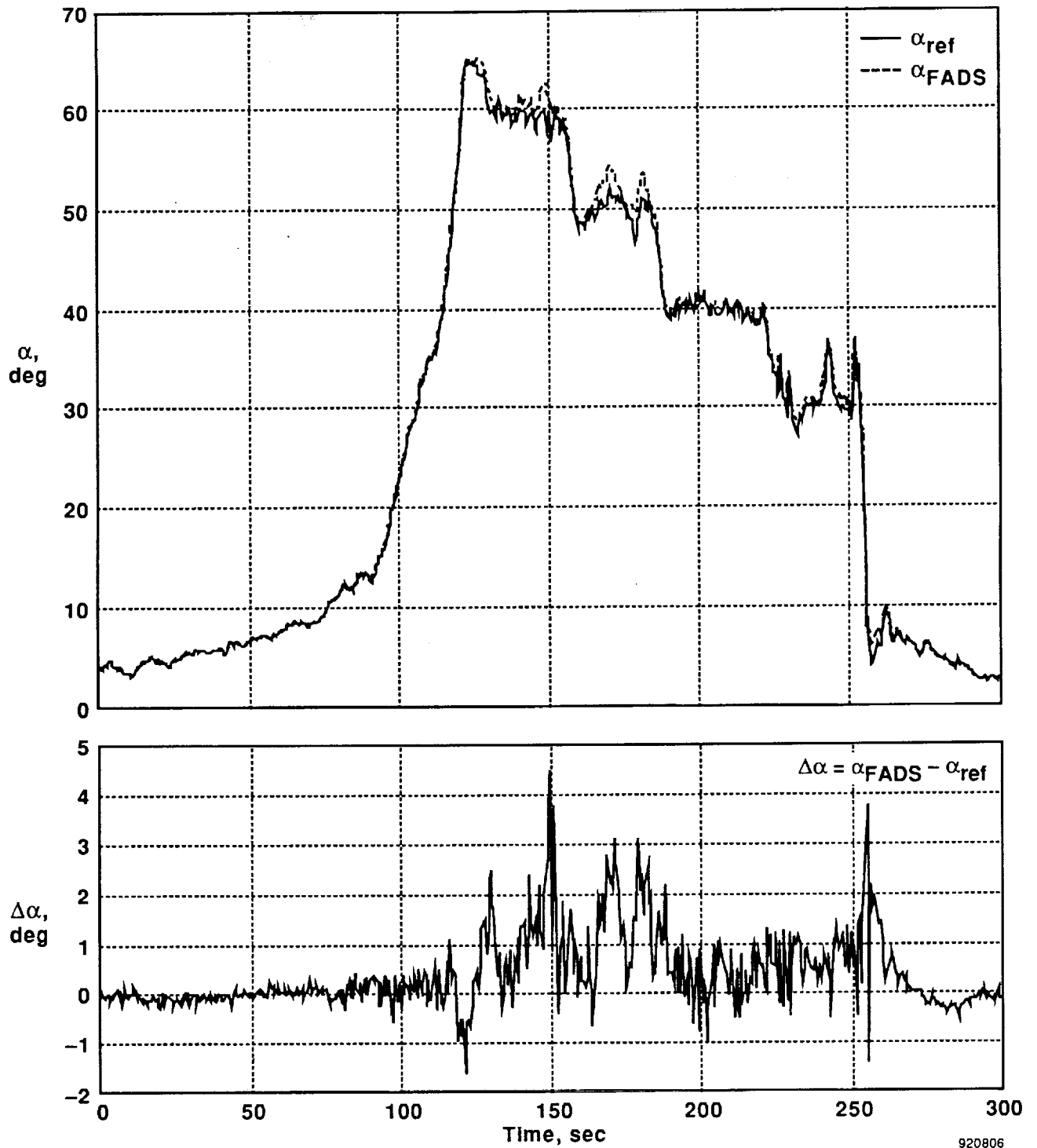
(d) Angle of attack.
Fig. 18 Continued.



920805

(e) Angle of sideslip.

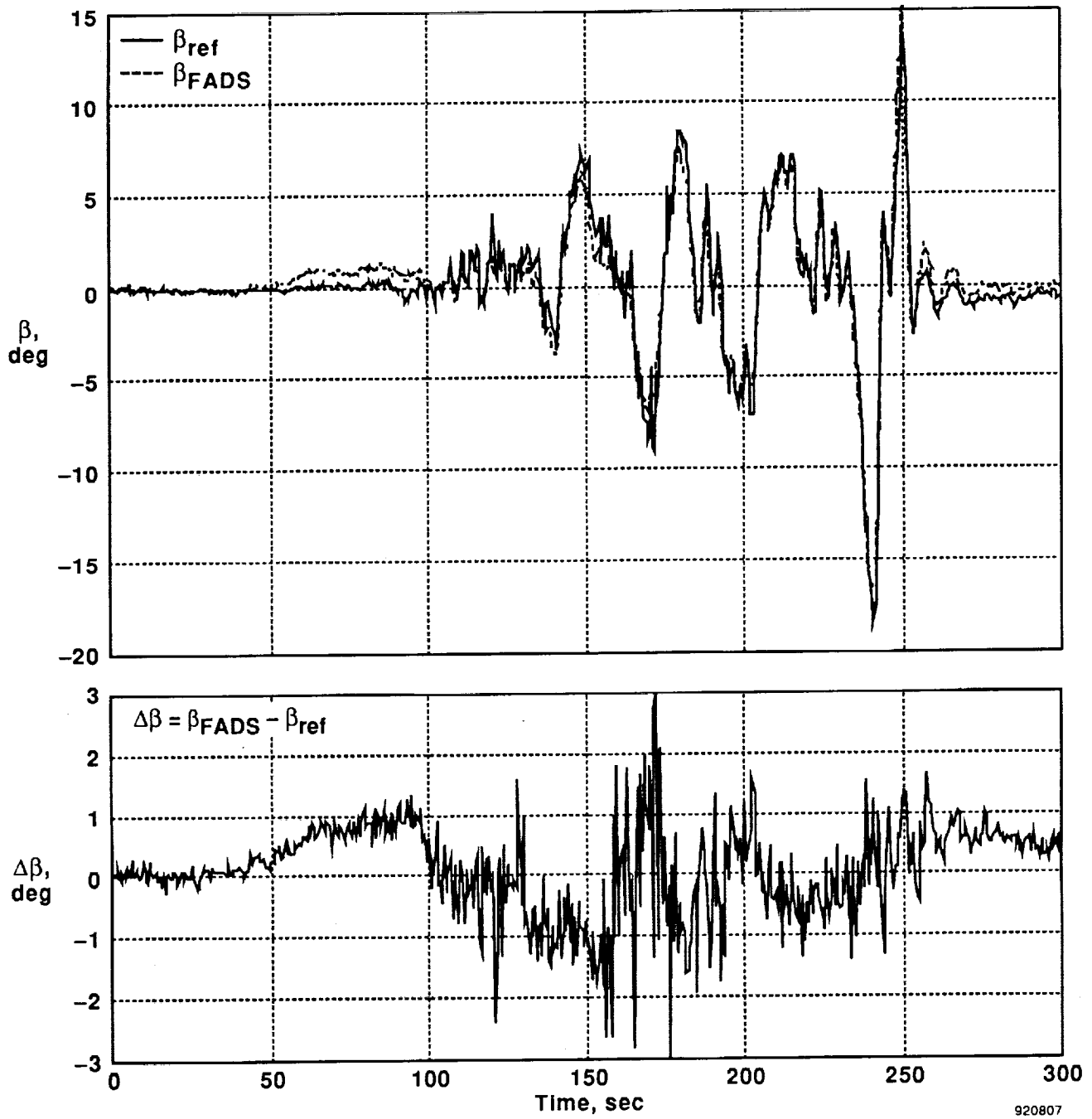
Fig. 18 Concluded.



920806

(a) Angle of attack.

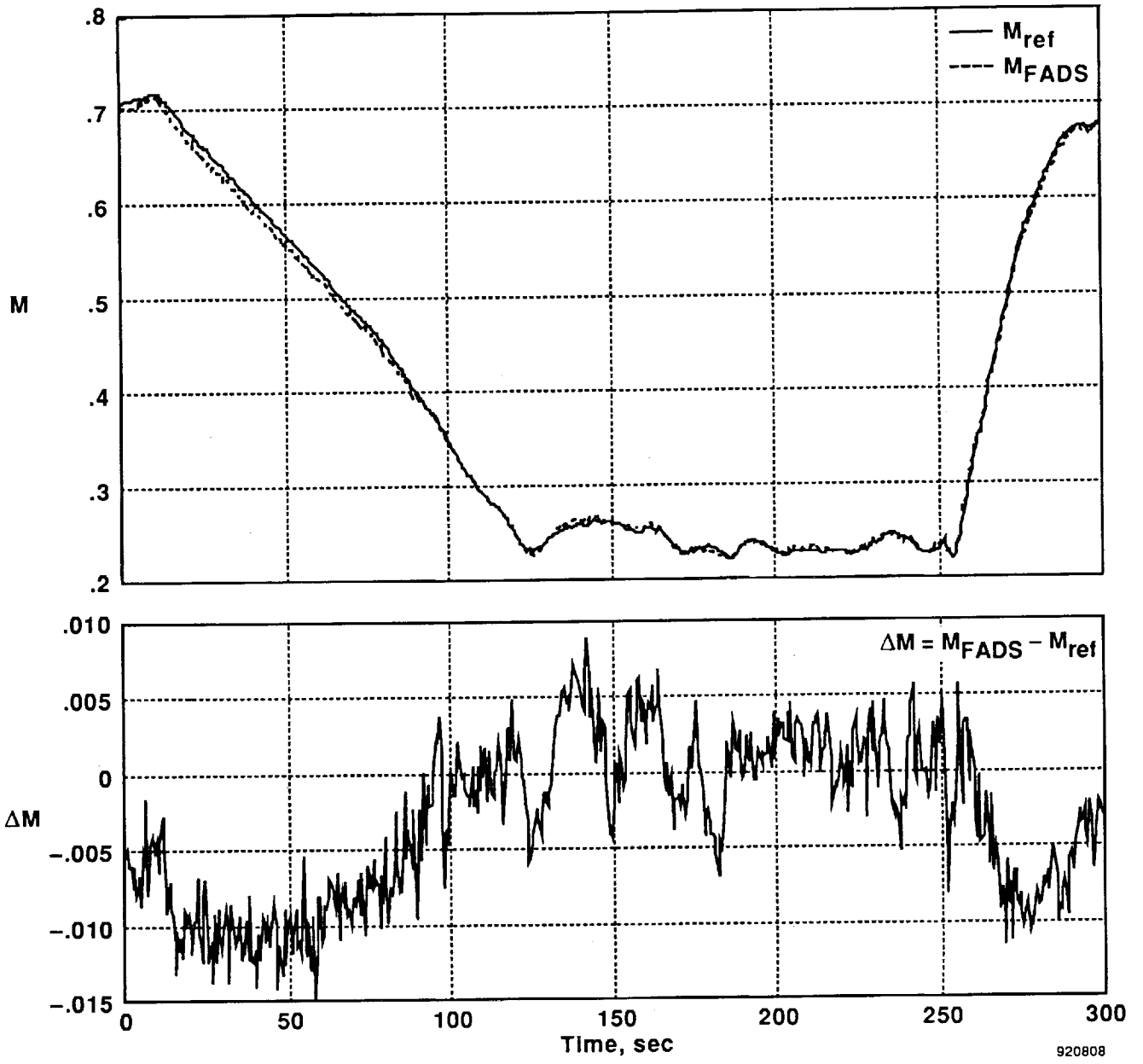
Fig. 19 Time histories for the high-angle-of-attack and sideslip maneuver.



920807

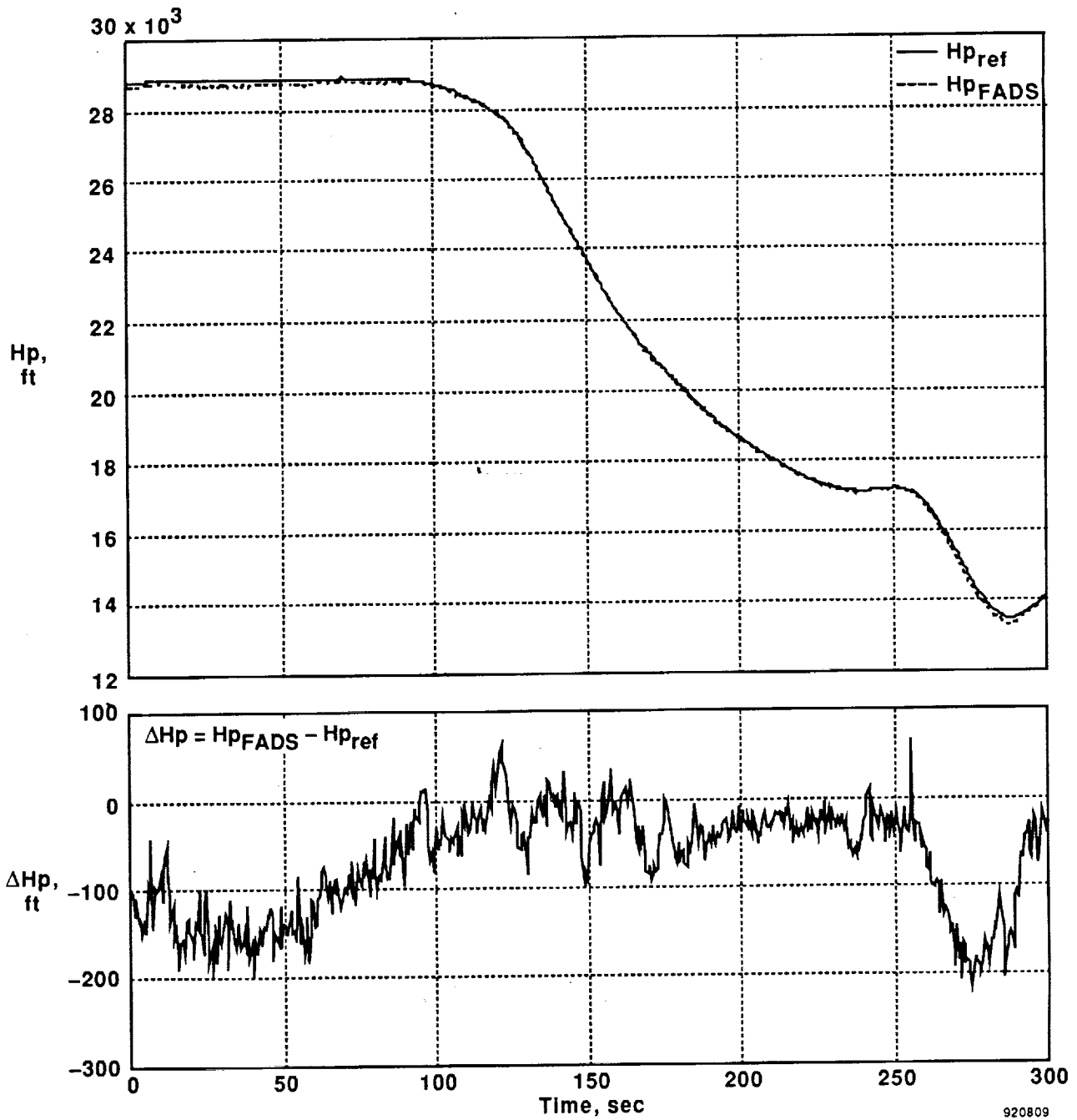
(b) Angle of sideslip.

Fig. 19 Continued.

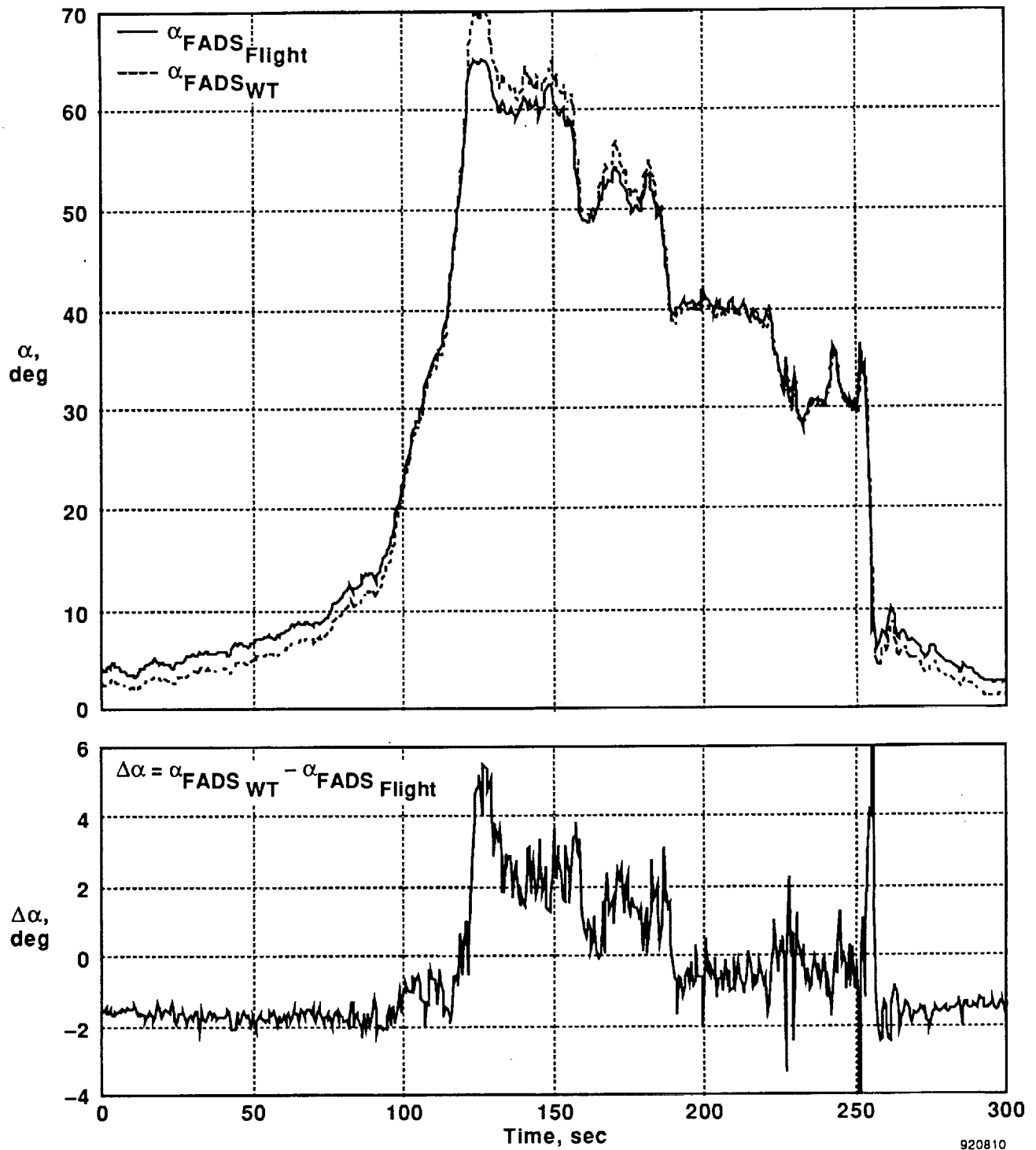


(c) Mach number.
 Fig. 19 Continued.

920808

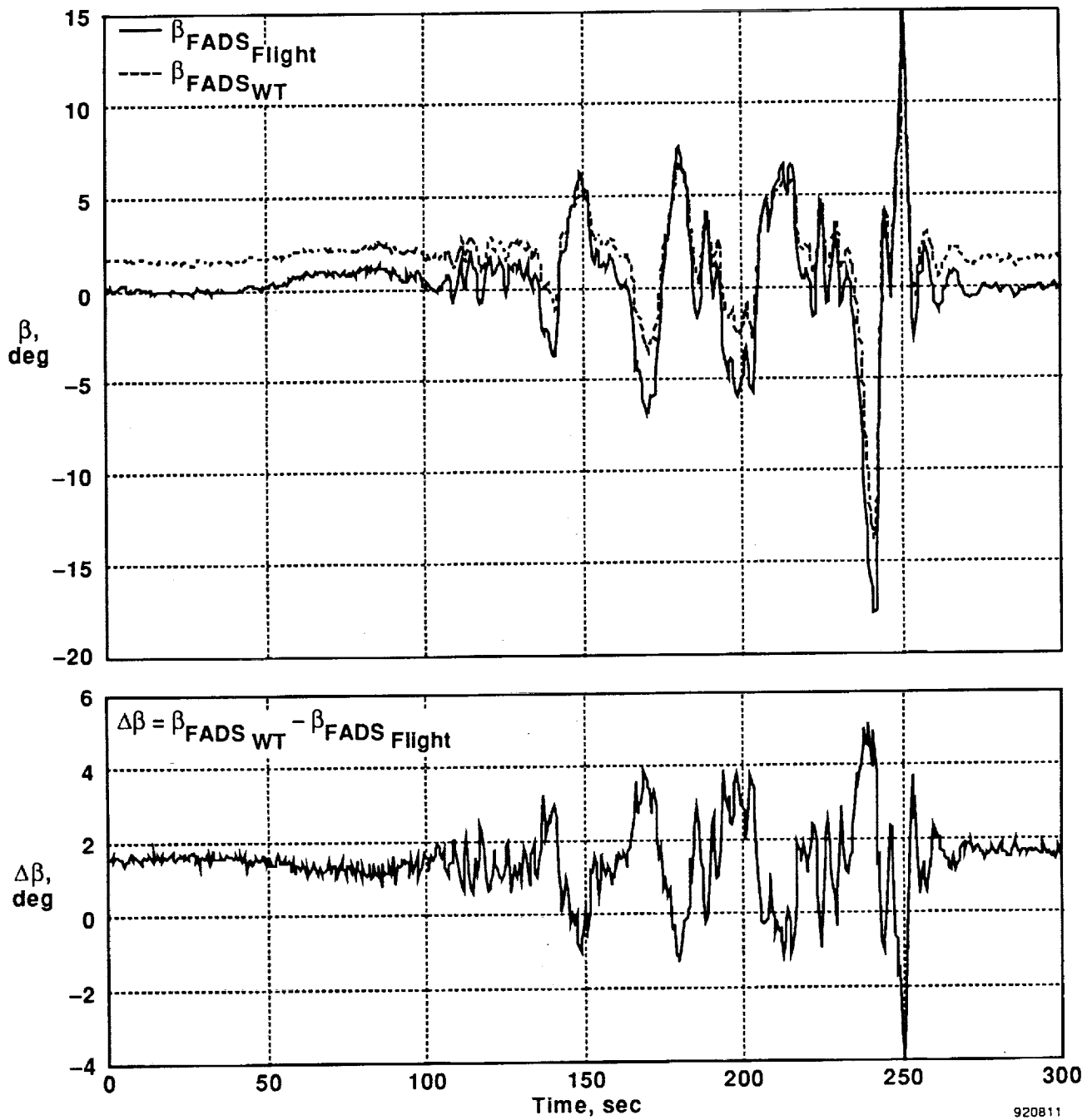


(d) Pressure altitude.
 Fig. 19 Concluded.



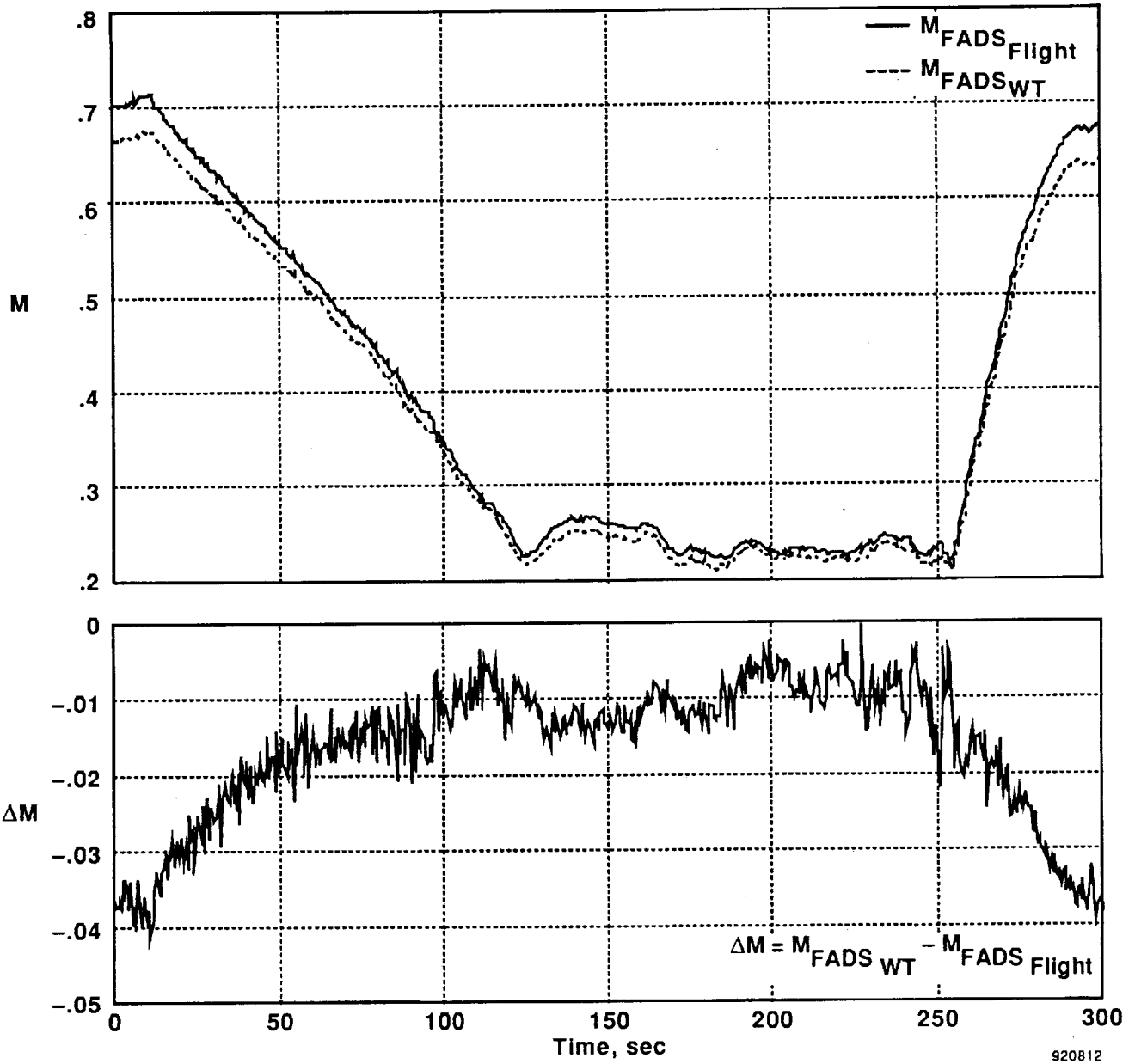
(a) Angle of attack.

Fig. 20 Comparison between flush airdata sensor calculations using wind-tunnel-derived and flight-derived calibrations.



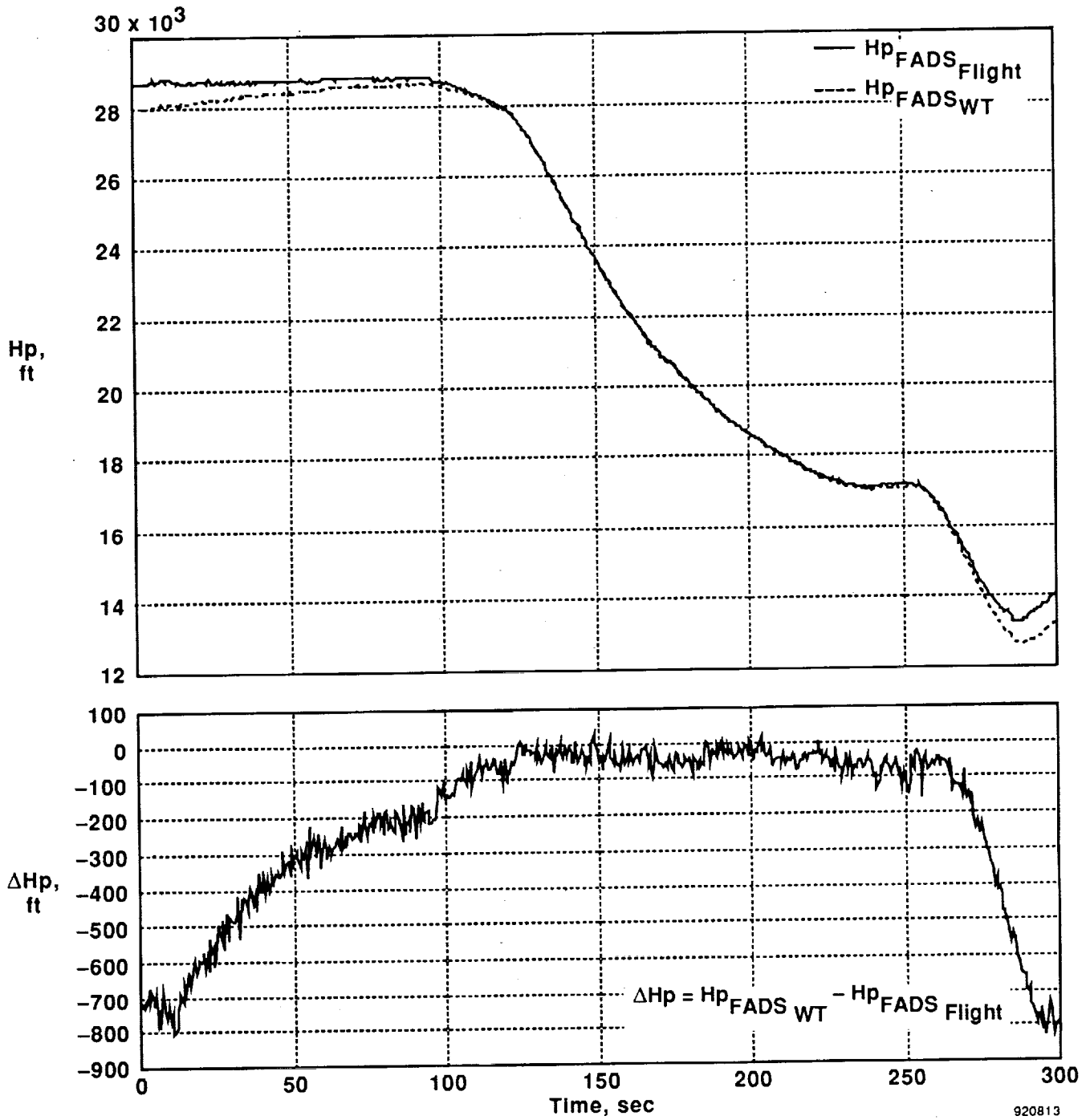
920811

(b) Angle of sideslip.
Fig. 20 Continued.



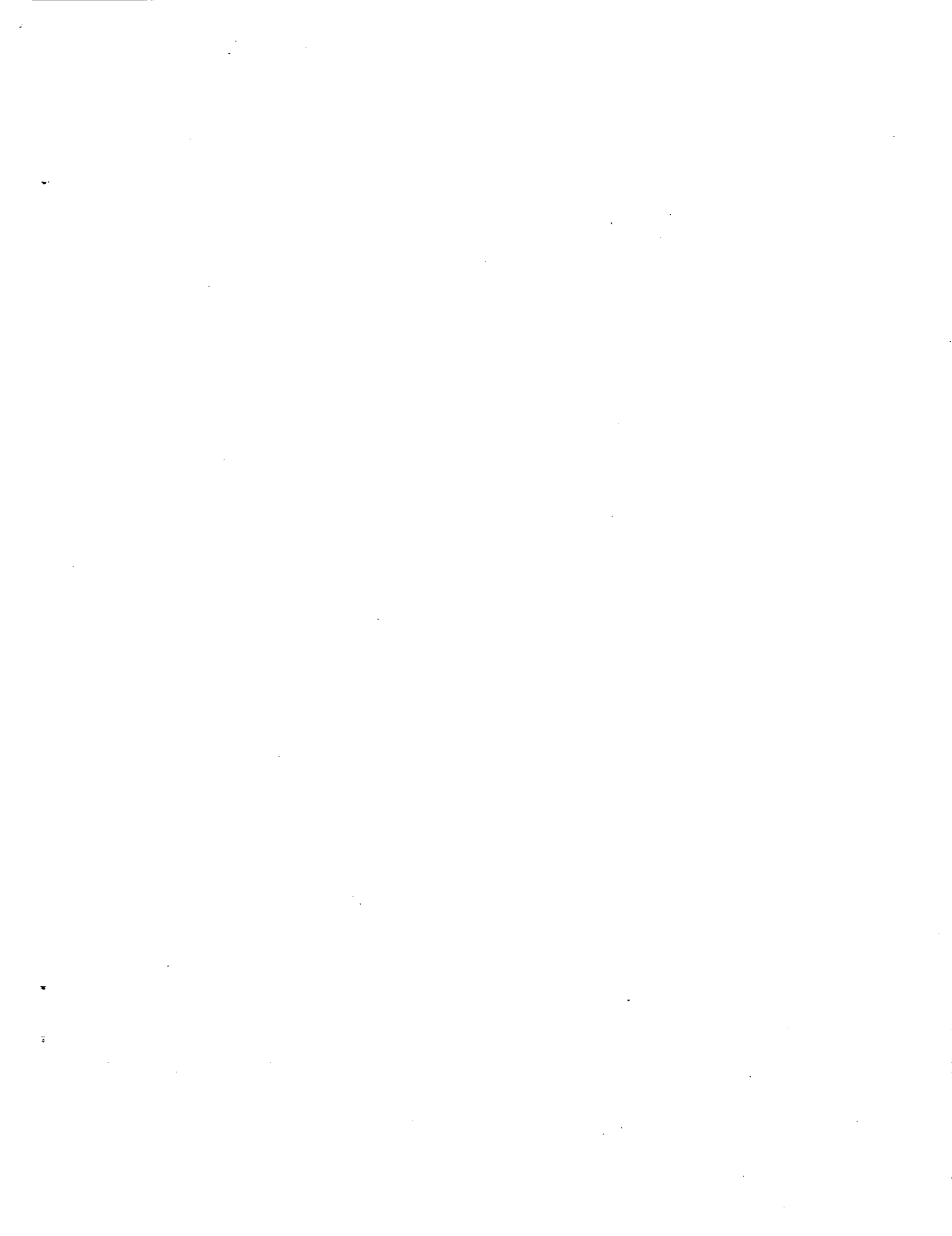
(c) Mach number.

Fig. 20 Continued.



(d) Pressure altitude.

Fig. 20 Concluded.



REPORT DOCUMENTATION PAGE

Form Approved
OMB No. 0704-0188

Public reporting burden for this collection of information is estimated to average 1 hour per response, including the time for reviewing instructions, searching existing data sources, gathering and maintaining the data needed, and completing and reviewing the collection of information. Send comments regarding this burden estimate or any other aspect of this collection of information, including suggestions for reducing this burden, to Washington Headquarters Services, Directorate for Information Operations and Reports, 1215 Jefferson Davis Highway, Suite 1204, Arlington, VA 22202-4302, and to the Office of Management and Budget, Paperwork Reduction Project (0704-0188), Washington, DC 20503.

1. AGENCY USE ONLY (Leave blank)	2. REPORT DATE February 1993	3. REPORT TYPE AND DATES COVERED Technical Memorandum	
4. TITLE AND SUBTITLE Flight and Wind-Tunnel Calibrations of a Flush Airdata Sensor at High Angles of Attack and Sideslip and at Supersonic Mach Numbers		5. FUNDING NUMBERS WU 505-68-30	
6. AUTHOR(S) Timothy R. Moes, Stephen A. Whitmore, and Frank L. Jordan, Jr.		8. PERFORMING ORGANIZATION REPORT NUMBER H-1875	
7. PERFORMING ORGANIZATION NAME(S) AND ADDRESS(ES) NASA Dryden Flight Research Facility P.O. Box 273 Edwards, California 93523-0273		10. SPONSORING/MONITORING AGENCY REPORT NUMBER NASA TM-104265	
9. SPONSORING/MONITORING AGENCY NAME(S) AND ADDRESS(ES) National Aeronautics and Space Administration Washington, DC 20546-0001		11. SUPPLEMENTARY NOTES Presented as AIAA-93-1017 at the AIAA/AHS/ASEE Aerospace Design Conference, February 16-19, 1993, Irvine, California.	
12a. DISTRIBUTION/AVAILABILITY STATEMENT Unclassified — Unlimited Subject Category 06		12b. DISTRIBUTION CODE	
13. ABSTRACT (Maximum 200 words) A nonintrusive airdata-sensing system has been calibrated in flight and wind-tunnel experiments to an angle of attack of 70° and to angles of sideslip of ±15°. Flight-calibration data have also been obtained to Mach 1.2. The sensor, known as the flush airdata sensor, has been installed on the nose-cap of an F-18 aircraft for flight tests and on a full-scale F-18 forebody for wind-tunnel tests. Flight tests occurred at the NASA Dryden Flight Research Facility, Edwards, California, using the F-18 High Alpha Research Vehicle. Wind-tunnel tests were conducted in the 30- by 60-ft wind tunnel at the NASA Langley Research Center, Hampton, Virginia. The sensor consists of 23 flush-mounted pressure ports arranged in concentric circles and located within 1.75 in. of the tip of the nose-cap. An overdetermined mathematical model was used to relate the pressure measurements to the local airdata quantities. The mathematical model was based on potential flow over a sphere and was empirically adjusted based on flight and wind-tunnel data. For quasi-steady maneuvering, the mathematical model worked well throughout the subsonic, transonic, and low supersonic flight regimes. The model also worked well throughout the angles-of-attack and -sideslip regions studied.			
14. SUBJECT TERMS Airdata; Airdata calibration; FADS; Flush airdata sensor; Nonintrusive airdata			15. NUMBER OF PAGES 31
17. SECURITY CLASSIFICATION OF REPORT Unclassified			16. PRICE CODE A03
18. SECURITY CLASSIFICATION OF THIS PAGE Unclassified	19. SECURITY CLASSIFICATION OF ABSTRACT Unclassified	20. LIMITATION OF ABSTRACT Unlimited	